

# Three-Dimensional Heterostructures of MoS<sub>2</sub> Nanosheets on Conducting MoO<sub>2</sub> as an Efficient Electrocatalyst To Enhance Hydrogen Evolution Reaction

Revannath Dnyandeo Nikam,<sup>†,‡,§,@</sup> Ang-Yu Lu,<sup>||,@</sup> Poonam Ashok Sonawane,<sup>⊥,#</sup> U. Rajesh Kumar,<sup>†,‡,§</sup> Kanchan Yadav,<sup>†,‡,§</sup> Lain-Jong Li,<sup>\*,||</sup> and Yit-Tsong Chen<sup>\*,†,‡</sup>

<sup>†</sup>Department of Chemistry, National Taiwan University, Taipei 106, Taiwan

<sup>‡</sup>Institute of Atomic and Molecular Sciences, Academia Sinica, Taipei 106, Taiwan

<sup>§</sup>Nanoscience and Technology Program, Taiwan International Graduate Program, Academia Sinica, Taipei 115, Taiwan

<sup>||</sup>Division of Physical Science & Engineering, King Abdullah University of Science and Technology, Thuwal 23955-6900, Kingdom of Saudi Arabia

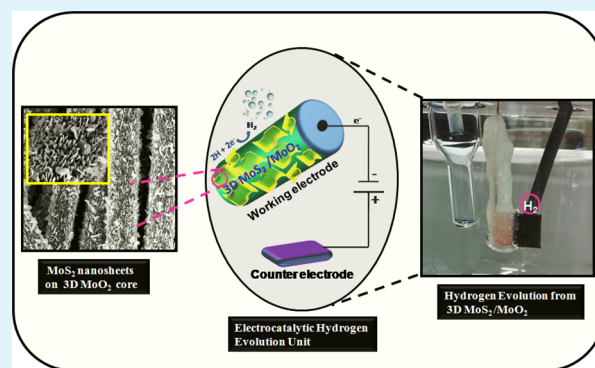
<sup>⊥</sup>Institute of Chemistry, Academia Sinica, Taipei 115, Taiwan

<sup>#</sup>Department of Applied Chemistry, National Chiao-Tung University, Hsinchu 300, Taiwan

## S Supporting Information

**ABSTRACT:** Molybdenum disulfide (MoS<sub>2</sub>) is a promising catalyst for hydrogen evolution reaction (HER) because of its unique nature to supply active sites in the reaction. However, the low density of active sites and their poor electrical conductivity have limited the performance of MoS<sub>2</sub> in HER. In this work, we synthesized MoS<sub>2</sub> nanosheets on three-dimensional (3D) conductive MoO<sub>2</sub> via a two-step chemical vapor deposition (CVD) reaction. The 3D MoO<sub>2</sub> structure can create structural disorders in MoS<sub>2</sub> nanosheets (referred to as 3D MoS<sub>2</sub>/MoO<sub>2</sub>), which are responsible for providing the superior HER activity by exposing tremendous active sites of terminal disulfur of S<sub>2</sub><sup>2-</sup> (in MoS<sub>2</sub>) as well as the backbone conductive oxide layer (of MoO<sub>2</sub>) to facilitate an interfacial charge transport for the proton reduction. In addition, the MoS<sub>2</sub> nanosheets could protect the inner MoO<sub>2</sub> core from the acidic electrolyte in the HER. The high activity of the as-synthesized 3D MoS<sub>2</sub>/MoO<sub>2</sub> hybrid material in HER is attributed to the small onset overpotential of 142 mV, a largest cathodic current density of 85 mA cm<sup>-2</sup>, a low Tafel slope of 35.6 mV dec<sup>-1</sup>, and robust electrochemical durability.

**KEYWORDS:** CVD growth, 3D heterostructures, MoS<sub>2</sub> nanosheets, 3D MoO<sub>2</sub> conductive core, electrocatalyst, hydrogen evolution reaction



## 1. INTRODUCTION

Due to the massive demand of energy, hydrogen fuel has been proposed as a main future energy resource.<sup>1–3</sup> Beyond the conventional hydrogen production, a lot of effort has been made recently to develop electrocatalytic and photocatalytic techniques to produce efficient hydrogen through the hydrogen evolution reaction (HER).<sup>4–7</sup> However, the existence of high operating overpotential for HER limits the practical applications of these techniques; therefore, developing high-performance catalysts to drive HER with minimum external energy is highly desirable. Platinum (Pt) is well-known for its superior electrocatalytic property; nevertheless, large-scale application of Pt-based technology is hindered by high cost and low availability. Hence, intensive research has recently been directed to search for earth abundant, low-cost potential substitutes for the Pt catalyst. Among the newly discovered catalysts, two-

dimensional layered transition metal dichalcogenides (TMDs) have emerged as promising electrocatalysts for HER.<sup>8–12</sup>

In TMDs, molybdenum disulfide (MoS<sub>2</sub>) has shown to be an excellent HER catalyst.<sup>8</sup> The computational and experimental results confirmed that the active catalytic sites of layered MoS<sub>2</sub> crystals are located at the sulfur edge, while basal planes are catalytically inert.<sup>13,14</sup> Notwithstanding, due to high surface energy and strong interlayer  $\pi$ - $\pi$  interaction, the inherent layer stacking and agglomeration in MoS<sub>2</sub> decrease the number of active sites.<sup>15</sup> In addition, the very poor electrical conductivity between two stacked S-Mo-S interlayers are about 2 orders of magnitude lower than that of intralayers.<sup>16,17</sup> Therefore,

Received: August 26, 2015

Accepted: October 5, 2015

Published: October 5, 2015

seeking advanced structural designs to engineer the morphological MoS<sub>2</sub> of more active sites for higher conductivity to enhance the electrocatalytic efficiency of MoS<sub>2</sub> in HER is highly demanded.

To overcome the conductivity barrier, MoS<sub>2</sub> has been grown on various conductive carbon-based substrates in recent years, such as graphene nanosheets,<sup>8</sup> 18N-doped graphene,<sup>19</sup> carbon nanotube,<sup>20,21</sup> carbon fiber,<sup>22</sup> carbon cloth,<sup>23</sup> three-dimensional (3D) hierarchical graphene oxide,<sup>24</sup> and graphene protected 3D Ni foam.<sup>25,26</sup> However, the direct deposition of MoS<sub>2</sub> on nonactive HER substrates would block the active sites of MoS<sub>2</sub>, thus significantly decreasing the HER activity. Alternatively, enormous effort has been taken to create efficient active sites by making different nanostructures of MoS<sub>2</sub>, such as mesopores,<sup>18</sup> chemically exfoliated 1T metallic nanosheets,<sup>27,28</sup> amorphous nanosheets,<sup>29–31</sup> oxygen-doped nanosheets,<sup>32,33</sup> defect-rich nanosheets,<sup>34</sup> nanowires,<sup>35</sup> monolayer 3D nonporous golds,<sup>36</sup> nanosheets on porous MoO<sub>2</sub>,<sup>37</sup> nitrogen-doped nanosheets on MoO<sub>2</sub> nanobelts,<sup>38</sup> and nanoparticles on TCNQ.<sup>39</sup> Among these, the recently developed phase-transfer strategy of producing metallic 1T MoS<sub>2</sub> from semiconductive 2H MoS<sub>2</sub> has significantly improved the HER activity due to the low resistance and high density of active sites in the metallic 1T MoS<sub>2</sub>. However, both the complicated synthetic procedures and the instability in the acidic electrolyte of 1T MoS<sub>2</sub> have made it less possible to become an ideal catalyst for HER. Although the previously reported morphological and structural modifications of MoS<sub>2</sub> are still insufficient to enhance the HER activity, an unprecedented 3D MoS<sub>2</sub>/MoO<sub>2</sub> hybrid material synthesized by controlling the conductivity and disorder in MoS<sub>2</sub> nanosheets coated on a 3D conductive MoO<sub>2</sub> core could make the practical implementation of MoS<sub>2</sub> for electrocatalytic hydrogen production in HER. The development of 3D architectures of the MoS<sub>2</sub>-based catalyst on a conducting substrate is of great interest due to their unique structure-dependent properties. More recently, a template-assisted wet-chemical approach to grow 3D MoS<sub>2</sub> on a conducting substrate has been developed, where the 3D assembled structures acted as an excellent catalyst for HER with high activity and stability.<sup>40,41</sup> Nevertheless, the mass production of such high-quality 3D architectures of MoS<sub>2</sub> demands a new method for large-scale synthesis. Herein, we propose an innovative approach to selectively grow a 3D heterostructure of MoS<sub>2</sub> on a conducting substrate, such as MoO<sub>2</sub>. The formation of such 3D heterostructures via a CVD reaction represents a completely new approach. In this paper, we demonstrate that the as-fabricated 3D hybrid heterostructures of MoS<sub>2</sub> nanosheets on a conductive MoO<sub>2</sub> core have several advantages to boost the HER activity. First, MoS<sub>2</sub> nanosheets act as a protective layer for the underlying 3D MoO<sub>2</sub> core from the environmental acidic electrolyte in HER, conferring the 3D MoS<sub>2</sub>/MoO<sub>2</sub> hybrid material higher stability. Second, the 3D MoS<sub>2</sub>/MoO<sub>2</sub> structure possesses a high specific surface area. Third, the underlying 3D conductive MoO<sub>2</sub> core allows the effective charge collection and charge transfer for a proton reduction reaction. Finally, the 3D MoO<sub>2</sub> architecture can create structural disorders in MoS<sub>2</sub> nanosheets, which are responsible for exposing tremendous active sites of terminal S<sub>2</sub><sup>2–</sup> to facilitate the HER.

## 2. EXPERIMENTAL SECTION

**2.1. Synthesis of 3D MoS<sub>2</sub>/MoO<sub>2</sub> Catalysts.** The 3D MoS<sub>2</sub>/MoO<sub>2</sub> heterostructures were synthesized in a low-pressure chemical

vapor deposition (LPCVD) reaction. The distorted MoS<sub>2</sub> nanosheets on metallic 3D MoO<sub>2</sub> were produced by low-temperature sulfurization in a two-step CVD process as illustrated in Figure 1. The commercially

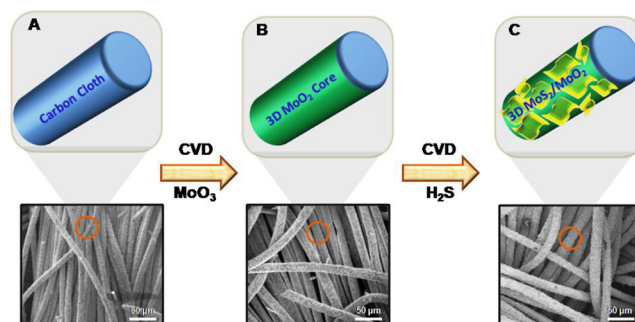


**Figure 1.** Schematic representations and SEM images illustrate a synthetic process of the designed MoS<sub>2</sub> nanosheets coated on a metallic 3D MoO<sub>2</sub> core, which is supported on carbon cloth, to be used as an electrode for HER. (A) Pristine carbon cloth, (B) metallic 3D MoO<sub>2</sub> on the carbon cloth via the CVD reaction of MoO<sub>3</sub>, and (C) MoS<sub>2</sub> nanosheets deposited on the metallic 3D MoO<sub>2</sub> core/carbon cloth (to form 3D MoS<sub>2</sub>/MoO<sub>2</sub>) by controlling the sulfurization of the pregrown MoO<sub>2</sub> core.

available carbon cloth (CeTech, W0S1002) was used as a template to grow metallic 3D MoO<sub>2</sub> cores. Before the synthesis, MoO<sub>3</sub> powder (Sigma-Aldrich, 99.995% 10 mg) as a chemical precursor was placed in a quartz boat close to the central heating zone of a furnace, where a carbon cloth substrate of 2 × 2 cm<sup>2</sup> was placed on top of the quartz boat containing the MoO<sub>3</sub> powder. Before starting the growth, highly pure Ar gas was purged into the furnace for 30 min to make the reaction chamber oxygen-free. The furnace was then heated to 650 °C at a heating rate of 25 °C/min. During the growth, the chamber pressure was maintained at 5 Torr with an Ar flow rate of 100 sccm. To form distorted MoS<sub>2</sub> nanosheets, the pregrown 3D MoO<sub>2</sub> cores supported by carbon cloth were sulfidized by hydrogen sulfide (H<sub>2</sub>S) gas at 100 Torr in another furnace with various reaction temperatures (200–1000 °C) under a ramp rate of 25 °C/min in a mixture of H<sub>2</sub>S (4 sccm)/Ar(1000 sccm) for 60 min.

**2.2. Structural Characterizations.** Powder X-ray diffraction (XRD) patterns of the as-synthesized samples were recorded by a Bruker D8 X-ray diffractometer with Cu K $\alpha$  ( $\lambda$  = 1.5406 Å) radiation in the  $2\theta$  range of 10–80°. Raman spectroscopy was used to identify the compositions of the samples with a confocal Raman microscope (NT-MDT, NTEGRA SPECTRA) and a liquid-nitrogen cooled charge-coupled device (CCD) camera. A laser at 488 nm with the spot size of  $\sim$ 1  $\mu$ m, adjusted by a 100 $\times$  objective lens, was used as an excitation source. To avoid sample damage and to gain better spectral resolution, the laser was adjusted to a medium power of 30 mW with the laser exposure time of 10 s. The Raman scattering signal of a silicon substrate at 520 cm<sup>–1</sup> was used as a reference for calibration. The surface morphologies of the samples were examined by scanning electron microscopy (FEI, Nova 200) equipped with an energy dispersive X-ray (EDX) spectrometer. The microstructural analysis was carried out using high-resolution transmission electron microscope (HRTEM, Tecnai F30) equipped with X-ray energy dispersive spectroscopy (EDS).

**2.3. Electrochemical Measurements.** Electrochemical studies were carried out in a 3-electrode cell using an AUTOLAB potentiostat (PGSTAT, 302N), where the as-prepared 3D MoS<sub>2</sub>/MoO<sub>2</sub> samples coated on a carbon cloth substrate served as the working electrode (WE), an Ag/AgCl (3.0 mol/kg KCl) was used as the reference electrode (RE), and a graphite rod worked as the counter electrode (CE). All of the electrochemical measurements were performed in 0.5 M H<sub>2</sub>SO<sub>4</sub> electrolyte. Linear sweep voltammetry was employed to obtain polarization plots with a fixed scan rate of 5 mV/s. The obtained polarization data were calibrated with respect to the

reversible hydrogen electrode (RHE) by  $E_{\text{RHE}} = E_{\text{SCE}} + 0.28$  V and were reported with an  $iR$  compensation by  $V_{\text{corr}} = V - jR_s$ , where  $V_{\text{corr}}$  is the corrected potential for  $iR$  drop,  $j$  is polarization current, and  $R_s$  is the series resistance. The electrochemical impedance spectra (EIS) were recorded in the frequency range of 102–105 Hz and at the applied amplitude of AC potential of 10 mV. The obtained experimental EIS data were fitted and deconvoluted to an equivalent circuit (2R-CPE circuit model using NOVA 1.9). The Nyquist and Bode plots were recorded from the fitted EIS results.

### 3. RESULTS AND DISCUSSION

The distorted  $\text{MoS}_2$  nanosheets on metallic 3D  $\text{MoO}_2$  were produced by low-temperature sulfurization in a two-step CVD process. Figure 1 illustrates the growth process and SEM images of the prepared 3D  $\text{MoS}_2/\text{MoO}_2$  hybrid structure, which involved two major steps. (A) Deposition of  $\text{MoO}_2$  cores on a carbon cloth substrate under an oxygen-free atmosphere to avoid the oxidation of  $\text{MoO}_2$ . (B) Formation of distorted  $\text{MoS}_2$  nanosheets via the stepwise sulfurization of the predeposited 3D  $\text{MoO}_2$  by  $\text{H}_2\text{S}$  under an inert Ar atmosphere. For tests, different samples were prepared at various sulfurization temperatures. The SEM images to display the carbon cloth,  $\text{MoO}_2$  cores on carbon cloth, and 3D  $\text{MoS}_2/\text{MoO}_2$  hybrid structures are shown in Figure 1. Briefly, the formation mechanism of the layered  $\text{MoS}_2/\text{MoO}_2$  structures is based on a controlled reduction and sulfurization process. In this method, underlying  $\text{MoO}_2$  cores were first synthesized on the 3D carbon cloth by the thermal reduction of  $\text{MoO}_3$  powder in an inert Ar atmosphere at 650 °C. The surface sulfurization of crystalline  $\text{MoO}_2$  cores by  $\text{H}_2\text{S}$  produces the top  $\text{MoS}_2$  nanosheets at various temperatures, where the efficiency of sulfurization depends on the diffusion rate of  $\text{H}_2\text{S}$  gas. Therefore, the structures and sizes of the underlying  $\text{MoO}_2$  cores and  $\text{MoS}_2$  nanosheets can be controlled via the layer-by-layer sulfurization by adjusting the sulfurization conditions.

Figure 2A shows the XRD patterns of the as-prepared samples of  $\text{MoO}_2$ , 3D  $\text{MoS}_2/\text{MoO}_2$ , and  $\text{MoS}_2$ . From the XRD patterns, it is clear that the sulfurization temperature has an important effect on the crystallinity of a catalyst. For the unsulfurized 3D  $\text{MoO}_2$  sample, Figure 2A(a) shows the pure

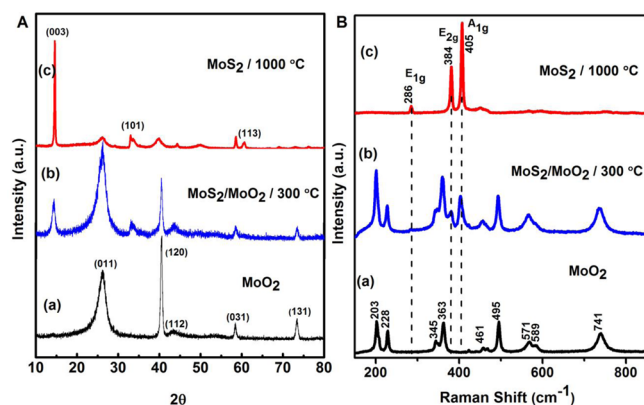


**Figure 2.** (A) XRD patterns of (a) the unsulfurized 3D  $\text{MoO}_2$  core with crystalline planes of  $\text{MoO}_2$ , (b) 3D  $\text{MoS}_2/\text{MoO}_2$  structure of both  $\text{MoS}_2$  and  $\text{MoO}_2$  crystals, and (c)  $\text{MoS}_2$  crystalline planes. (B) Raman spectra recorded under 488 nm excitation for (a) the unsulfurized 3D  $\text{MoO}_2$  core, (b) 3D  $\text{MoS}_2/\text{MoO}_2$  core where the appearance of new bands are attributed to  $\text{MoS}_2$  as marked by dashed lines, and (c) pure  $\text{MoS}_2$  with the identified  $E_{1g}$ ,  $E_{2g}$ , and  $A_{1g}$  phonon modes.

crystalline  $\text{MoO}_2$  (JCPDS:32-0671, monoclinic) with the characteristic diffraction peaks at 40° (120), 43° (112), 58° (031), and 73° (131). As the sulfurization temperature was raised to 300 °C [Figure 2A(b)], in addition to  $\text{MoO}_2$ , several medium-weak peaks appeared at 14.3°, 33.1°, and 60.4°, corresponding to  $\text{MoS}_2$  (003), (101), and (113), respectively (JCPDS: 65-3656, hexagonal). These results suggest that the 3D  $\text{MoS}_2/\text{MoO}_2$  hybrid structure could be formed at 300 °C. Figure 2A(c) further shows that pure  $\text{MoS}_2$  was obtained at 1000 °C, where only the diffraction peaks at 14.3° (003), 33.1° (101), and 60.4° (113) were observed, indicating the disappearance of the  $\text{MoO}_2$  core. These results demonstrate that the transition of 3D  $\text{MoS}_2/\text{MoO}_2$  to crystalline  $\text{MoS}_2$  can be adjusted by the sulfurization temperature.

The as-prepared samples were also characterized by Raman spectroscopy as shown in Figure 2B. Thermal deposition of  $\text{MoO}_3$  on the carbon cloth substrate leads to the formation of metallic  $\text{MoO}_2$  cores through the thermal reduction of  $\text{MoO}_3$ . In Figure 2B(a), Raman signals of the unsulfurized 3D metallic  $\text{MoO}_2$  core comprise those of the reported rutile  $\text{MoO}_2$  crystal,<sup>42</sup> where the peaks at 203–495  $\text{cm}^{-1}$  are assigned to the stretching modes of the doubly coordinated oxygen ( $\text{Mo}-\text{O}-\text{Mo}$ ) and the signals at 571, 589, and 741  $\text{cm}^{-1}$  are due to the stretching modes of terminal oxygen ( $\text{M}=\text{O}$ ). This Raman identification of the unsulfurized  $\text{MoO}_2$  sample suggests the presence of tetrahedral co-ordination on the  $\text{Mo}^{2+}$  (i.e., metallic 3D  $\text{MoO}_2$ ) center, which is subjected to sulfurization by  $\text{H}_2\text{S}$  at various temperatures from 200 to 1000 °C. When the sulfurization temperature was increased to 300 °C [Figure 2B(b)], accompanying with the original signals of  $\text{MoO}_2$  are new emerging peaks at ~384 and 405  $\text{cm}^{-1}$ , corresponding to the  $E_{1g}$  (the in-plane vibration of the S atoms) and  $A_{1g}$  (the out-of-plane vibration of the S atoms) modes of  $\text{MoS}_2$ , respectively.<sup>43</sup> This outcome confirms that the partial sulfurization of 3D  $\text{MoO}_2$  core occurred at 300 °C, leading to the formation of the 3D  $\text{MoS}_2/\text{MoO}_2$  hybrid structure. At higher sulfurization temperature of 1000 °C [Figure 2B(c)], all peaks of the  $\text{MoO}_2$  core disappeared, transforming to the complete formation of  $\text{MoS}_2$  on the carbon cloth substrate. The detailed spectral analyses of the observed Raman bands are listed in Table S1.

The surface morphologies of  $\text{MoO}_2$ , 3D  $\text{MoS}_2/\text{MoO}_2$ , and  $\text{MoS}_2$  on carbon cloth were further investigated by scanning electron microscopy (SEM). Figure 3A shows the high- and low-magnification SEM images of 3D  $\text{MoO}_2$  cores, indicating that the entire surface of the carbon cloth was uniformly covered with  $\text{MoO}_2$  cores of ~100 nm in thickness. After the sulfurization temperature was increased to 300 °C, it can be seen from Figure 3B that the  $\text{MoO}_2$  surfaces were decorated with  $\text{MoS}_2$  nanosheets of ~22 nm in thickness and ~50 nm in length. This result provides a strong evidence of forming distorted  $\text{MoS}_2$  nanosheets on the 3D  $\text{MoO}_2$  core. As revealed from Figure 3C, the distorted  $\text{MoS}_2$  nanosheets were converted into continuous  $\text{MoS}_2$  layers by raising the sulfurization temperature to 1000 °C and the  $\text{MoO}_2$  cores also turned completely into  $\text{MoS}_2$  layers. In Figure 3D, the SEM image and EDX elemental mappings of the as-prepared 3D  $\text{MoS}_2/\text{MoO}_2$  hybrid structure obtained at 300 °C reveal uniform distributions of the Mo, O, and S elements. In comparison, while the EDX mapping of the unsulfurized  $\text{MoO}_2$  in Figure S1 contains the elements of Mo and O, the  $\text{MoS}_2$  sample was obtained only at 1000 °C as shown in Figure S2. The results from EDX elemental mapping are consistent with those



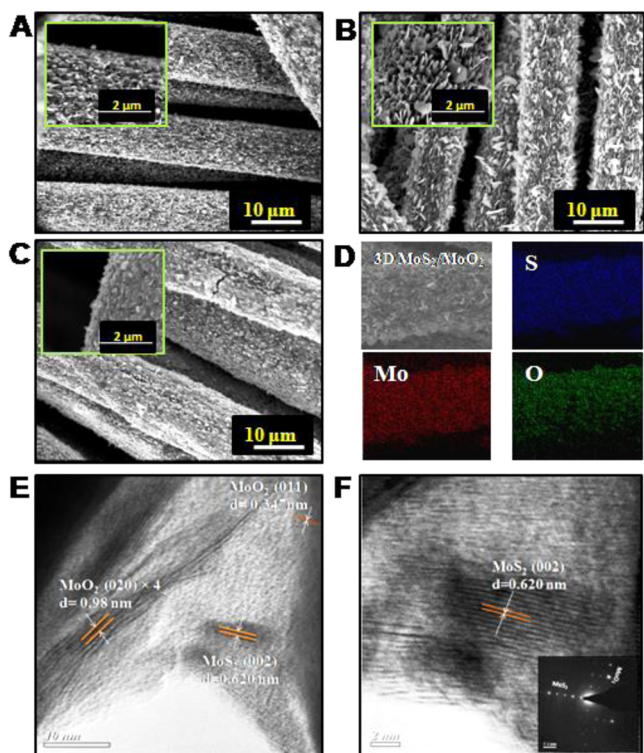


**Figure 3.** SEM images of (A) MoO<sub>2</sub> on carbon cloth synthesized at 650 °C, (B) 3D MoS<sub>2</sub>/MoO<sub>2</sub> on carbon cloth synthesized at 300 °C, and (C) MoS<sub>2</sub> on carbon cloth synthesized at 1000 °C. All insets in (A–C) show the corresponding high-magnification SEM images. (D) EDX elemental mapping images of Mo, S, and O for the 3D MoS<sub>2</sub>/MoO<sub>2</sub>. (E) HRTEM image of the 3D MoS<sub>2</sub>/MoO<sub>2</sub>. (F) HRTEM image of a selected MoS<sub>2</sub> region. The inset shows a selected-area electron diffraction (SAED) pattern for the 3D MoS<sub>2</sub>/MoO<sub>2</sub>.

obtained from XRD and Raman spectroscopy. Microstructural characterization of the 3D MoS<sub>2</sub>/MoO<sub>2</sub> heterostructures was performed with HRTEM. Figure 3E displays an HRTEM image of the 3D MoS<sub>2</sub>/MoO<sub>2</sub> heterostructure, where MoS<sub>2</sub> layers grew vertically on the 3D MoO<sub>2</sub> backbone. Figure 3F shows an HRTEM image taken in the middle of this 3D MoS<sub>2</sub>/MoO<sub>2</sub> heterostructure. Several sheet-like MoS<sub>2</sub> layers of ~20 nm in length and several nanometers in width were observed to be closely packed on the top of MoO<sub>2</sub> layers. The HRTEM image of a selected MoS<sub>2</sub> region (Figure 3E) reveals the individual atomic planes ordered in the S–Mo–S sequence for the layer formation. The layer spacings can be determined to be ~0.620 nm for MoS<sub>2</sub> (002), ~0.980 nm for MoO<sub>2</sub> (020 × 4), and ~0.347 nm for MoO<sub>2</sub> (011), which are in good agreement with the lattice spacings of MoS<sub>2</sub> and MoO<sub>2</sub> crystals.<sup>37</sup> To provide a further insight into the structural and morphological features of the obtained 3D MoO<sub>2</sub> core, transmission electron microscopic (TEM) characterizations were performed. Figure S3A and S3B show the low-magnification TEM images for the detached MoO<sub>2</sub> core from the carbon cloth by ultrasonication. It is interesting that spiral 3D morphological ultrathin layers of MoO<sub>2</sub> cores were observed after detaching from the 3D template.

To investigate the valence states and surface chemical compositions of MoO<sub>2</sub>, 3D MoS<sub>2</sub>/MoO<sub>2</sub>, and MoS<sub>2</sub>, high-resolution X-ray photoemission spectroscopy (XPS) was performed. Figure 4 shows the XPS spectra scanned in the Mo 3d and S 2p regions of MoO<sub>2</sub>, 3D MoS<sub>2</sub>/MoO<sub>2</sub>, and MoS<sub>2</sub>.

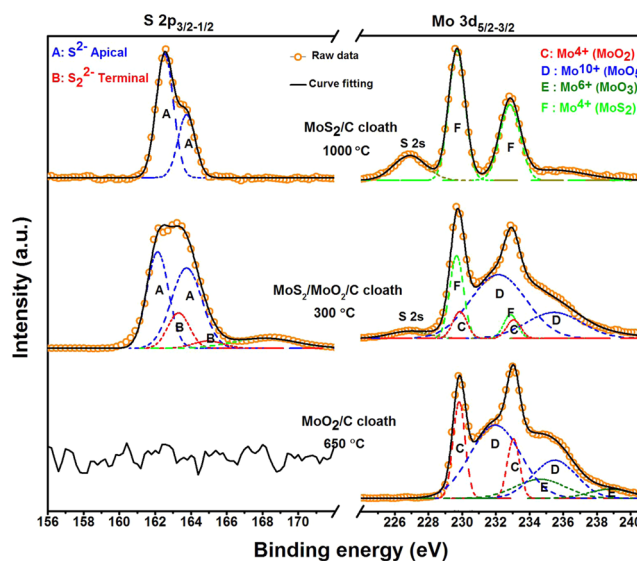


**Figure 4.** XPS spectra at high-resolution scans of the Mo 3d<sub>5/2-3/2</sub> and S 2p<sub>3/2-1/2</sub> regions for the 3D MoO<sub>2</sub>, 3D MoS<sub>2</sub>/MoO<sub>2</sub>, and MoS<sub>2</sub> catalysts grown on carbon cloth. In the S 2p<sub>3/2-1/2</sub> region, the doublet A, corresponding to the apical S<sup>2-</sup> at the lower-energy side (162.1–163.3 eV), partially overlap the doublet B, attributed to the bridging S<sup>2-</sup> at the higher-energy side (163.7–164.9 eV). In the Mo 3d<sub>5/2-3/2</sub> region, the doublet C is due to the Mo<sup>4+</sup> in MoO<sub>2</sub> (229.8–233.04 eV), doublet D is Mo<sup>10+</sup> in MoO<sub>5</sub> (231.9–234.6 eV), doublet E is Mo<sup>6+</sup> in MoO<sub>3</sub> (235.4–238.7 eV), and doublet F is Mo<sup>4+</sup> in MoS<sub>2</sub> (229.6–232.8 eV).

It is well-known that the apical divalent sulfide ions (S<sup>2-</sup>) in MoS<sub>2</sub> act as active sites in HER;<sup>31,44</sup> moreover, recent studies reported that the presence of terminal S<sup>2-</sup>, in addition to S<sup>2-</sup>, boosts the HER activity. In XPS spectra, the S 2p<sub>3/2</sub> and 2p<sub>1/2</sub> signals of terminal S<sup>2-</sup> (denoted by doublet B) at 163.7–164.9 eV are located at higher binding energies than those of apical S<sup>2-</sup> (represented as doublet A) at 162.1–163.3 eV.<sup>14,45</sup> In Figure 4, the MoO<sub>2</sub> core to facilitate the formation of apical S<sup>2-</sup> ions is confirmed by the presence of doublet A in XPS spectra, where the signals were deconvoluted. The analysis from Figure 4 shows that 3D MoS<sub>2</sub>/MoO<sub>2</sub> has both terminal S<sup>2-</sup> (doublet B) and apical S<sup>2-</sup> (doublet A). It is interesting to observe that the signals of S<sup>2-</sup> (doublet B) almost disappeared in MoS<sub>2</sub> because of the high crystalline phase of MoS<sub>2</sub>. Also in Figure 4, the unsulfidized MoO<sub>2</sub> sample does not possess S<sup>2-</sup> and S<sup>2-</sup>. The ratios of apical S<sup>2-</sup> to terminal S<sup>2-</sup> for MoO<sub>2</sub>, 3D MoS<sub>2</sub>/MoO<sub>2</sub>, and MoS<sub>2</sub> are summarized in Table S2. These XPS results suggest that the presence of terminal S<sup>2-</sup> could be the main cause to enhance the HER activity in 3D MoS<sub>2</sub>/MoO<sub>2</sub>.

In the XPS analysis, the Mo 3d orbital splits into 3d<sub>5/2</sub> (higher energy) and 3d<sub>3/2</sub> (lower energy) due to the spin–orbital splitting. In MoO<sub>2</sub>, the doublets are at 229.8 eV for Mo<sup>4+</sup> 3d<sub>5/2</sub> and at 233.04 eV for Mo<sup>4+</sup> 3d<sub>3/2</sub>.<sup>46</sup> After the complete reduction of MoO<sub>3</sub>, the characteristic doublets at 235.4–238.7 eV for MoO<sub>3</sub> were not observed; however, due to the slight surface oxidation of the metastable MoO<sub>2</sub> in air, doublets for the Mo<sup>6+</sup> (235.4–238.7 eV) of MoO<sub>3</sub> were detected.<sup>47,48</sup> In the 3d regions of the Mo ions, the main 3d<sub>5/2</sub> and 3d<sub>3/2</sub> peaks were further analyzed with several doublets of Mo<sup>4+</sup> (peak C, at 229.8–233.04 eV) for MoO<sub>2</sub>, Mo<sup>10+</sup> (peak D, at 231.9–234.6 eV) for MoO<sub>5</sub>, Mo<sup>4+</sup> (peak E, at 229.6–232.8 eV) for MoS<sub>2</sub>, and Mo<sup>6+</sup> (peak F, at 235.4–238.7 eV) for MoO<sub>3</sub>. Each doublet was deconvoluted with a fixed peak

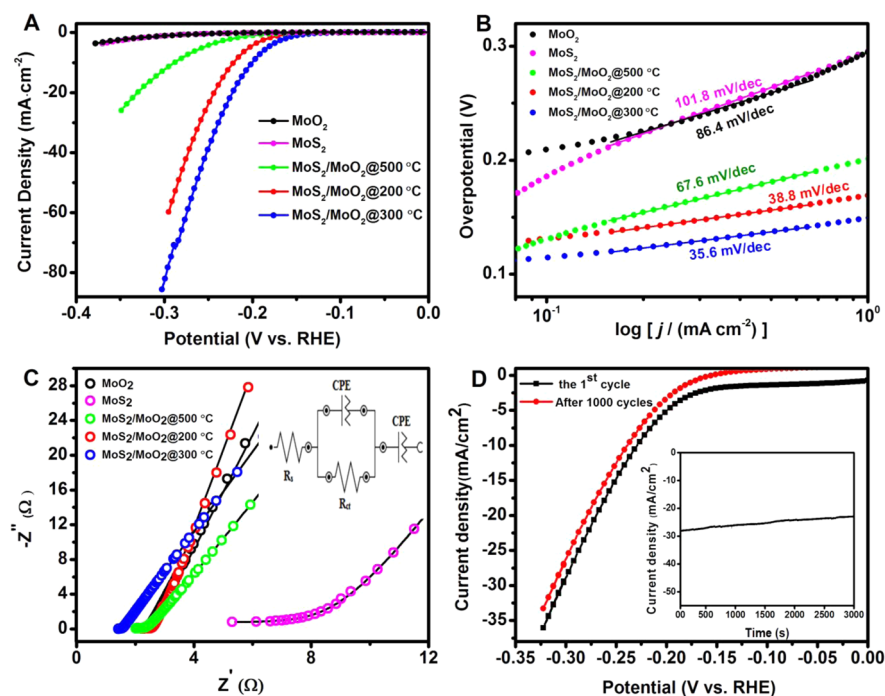


**Figure 5.** (A) The  $iR$  corrected polarization curves recorded at the scan rate of  $5 \text{ mV s}^{-1}$  for the HER containing  $0.5 \text{ M H}_2\text{SO}_4$  with the unsulfidized  $3\text{D MoO}_2$ ,  $3\text{D MoS}_2/\text{MoO}_2$  (prepared at  $200^\circ\text{C}$  CVD),  $3\text{D MoS}_2/\text{MoO}_2$  (prepared at  $300^\circ\text{C}$  CVD),  $3\text{D MoS}_2/\text{MoO}_2$  (prepared at  $500^\circ\text{C}$  CVD), and  $\text{MoS}_2$ , respectively. (B) The corresponding Tafel plots with the data being derived from (A). (C) The Nyquist plots and an equivalent circuit of the unsulfidized  $\text{MoO}_2$ ,  $3\text{D MoS}_2/\text{MoO}_2$  ( $200^\circ\text{C}$ ),  $3\text{D MoS}_2/\text{MoO}_2$  ( $300^\circ\text{C}$ ),  $3\text{D MoS}_2/\text{MoO}_2$  ( $500^\circ\text{C}$ ), and  $\text{MoS}_2$  at a potential of  $-200 \text{ mV}$  (vs RHE). (D) Stability test for the  $3\text{D MoS}_2/\text{MoO}_2$  ( $300^\circ\text{C}$ ).

separation of  $3.2 \text{ eV}$ , intensity ratio ( $3d_{5/2}: 3d_{3/2}$ ) of  $3:2$ , and the same full width at half-maximum (FWHM).

The XPS results for the unsulfidized  $\text{MoO}_2$  sample (Figure 4) clearly show that peak intensities for the reduced states of  $\text{Mo}^{4+} 3d_{3/2}$  and  $3d_{5/2}$  from  $\text{MoO}_2$  (peak C) and of  $\text{Mo}^{10+} 3d_{3/2}$  and  $3d_{5/2}$  from  $\text{MoO}_5$  (peak D) are much higher than those of  $\text{Mo}^{6+} 3d_{3/2}$  and  $3d_{5/2}$  of  $\text{MoO}_3$  (peak E), suggesting a complete reduction of  $\text{MoO}_3$  to  $\text{MoO}_2$ . Similarly, Figure 4 also presents the  $3d$  Mo regions for  $3\text{D MoS}_2/\text{MoO}_2$  and  $\text{MoS}_2$ . In both spectra, the new  $\text{S } 2s$  peak at  $226.7 \text{ eV}$  (peak F) belongs to  $\text{MoS}_2$ , indicating the formation of  $\text{MoS}_2$ . For  $3\text{D MoS}_2/\text{MoO}_2$  sample, fractional percentages of the oxidation states of  $+4$  ( $\text{MoO}_2$ ),  $+10$  ( $\text{MoO}_5$ ),  $+4$  ( $\text{MoS}_2$ ), and  $+6$  ( $\text{MoO}_3$ ) were measured to be  $8.04\%$ ,  $61.89\%$ ,  $18.3\%$ , and  $8.31\%$ , respectively, which confirmed the formation of the  $\text{MoS}_2/\text{MoO}_2$  core. In the formation of  $\text{MoS}_2$ , while the fractional percentages of  $+4$  ( $\text{MoO}_2$ ),  $+10$  ( $\text{MoO}_5$ ), and  $+6$  ( $\text{MoO}_3$ ) reduced to  $0\%$ ,  $0\%$ , and  $16.09\%$ , respectively, the intensity of  $+4$  ( $\text{MoS}_2$ ) increased to  $68.73\%$ . In Table S3, the ratios of  $\text{Mo}^{4+} (\text{MoS}_2)/\text{Mo}^{4+} (\text{MoO}_2)$  and of  $\text{Mo}^{4+} (\text{MoO}_2)/\text{Mo}^{6+} (\text{MoO}_3)$  were estimated for all samples. Additionally, the results obtained from the XPS analysis are summarized in Figure S4 and are also correlated with the results collected from the EDX spectral analysis in Figure S5. The results obtained from XPS, consistent well with those of EDX, clearly show that the formation of  $\text{MoS}_2$  on the  $3\text{D MoO}_2$  core through sulfurization was carried out at  $300^\circ\text{C}$ , of which the as-prepared samples possess high percentage of active sites of apical  $\text{S}^{2-}$  and terminal  $\text{S}_2^{2-}$ . Additionally, the structure and composition of the  $3\text{D MoS}_2/\text{MoO}_2$  prepared at  $500^\circ\text{C}$  were investigated by SEM, EDX, and XPS. The observed SEM (Figure S6A) shows that parts of the sample peeled off from the original substrate due to the high sulfurization rate and reveals that almost all of the underlying

$\text{MoO}_2$  was converted to  $\text{MoS}_2$ . The XPS analyses (Figure S6, F–G) on both  $\text{Mo } 3d$  and  $\text{S } 2p$  regions indicate that this sample contains  $+10$  ( $\text{MoO}_5$ ),  $+4$  ( $\text{MoS}_2$ ), and apical  $\text{S}^{2-}$ , which are consistent with the EDX examination (Figures S6, B–D).

The electrocatalytic HER activities for the samples prepared above were conducted in a 3-electrode cell containing  $0.5 \text{ M H}_2\text{SO}_4$ . Figure 5A shows the polarization curve of the HER between  $-0.4$  and  $0.0 \text{ V}$  vs RHE ( $iR$  corrected) at the scan rate of  $5 \text{ mV/s}$  for  $\text{MoO}_2$ ,  $3\text{D MoS}_2/\text{MoO}_2$ , and  $\text{MoS}_2$ , which were deposited on the carbon cloth with the same loading of  $\sim 0.30 \text{ mg/cm}^2$ . While the unsulfidized  $\text{MoO}_2$  and the completely sulfidized  $\text{MoS}_2$  exhibited poor catalytic activity for HER (with small cathodic currents at  $\eta = 300 \text{ mV}$ ), the as-prepared  $3\text{D MoS}_2/\text{MoO}_2$  (at  $300^\circ\text{C}$ ) hybrid electrode could provide an extremely large cathodic current density of  $85 \text{ mA cm}^{-2}$  at  $\eta = 300 \text{ mV}$ . As shown in Figure S7, compared with  $\text{MoO}_2$  and  $\text{MoS}_2$ ,  $3\text{D MoS}_2/\text{MoO}_2$  holds a much lower onset potential of  $142 \text{ mV}$ . This small onset potential and higher cathodic current density yield a superior HER activity, which can be attributed to the distorted structures of  $\text{MoS}_2$  nanosheets assembled on the metallic  $3\text{D MoO}_2$  core. It is widely accepted that the HER active sites are located on the edge planes; therefore, the HER activity can be greatly enhanced by tailoring the  $\text{MoS}_2$  microstructures to obtain highly exposed edge planes.<sup>49,50</sup> In the present case, the distorted  $\text{MoS}_2$  nanosheets assembled on the  $3\text{D MoO}_2$  core possess much more exposed edge planes than pure  $\text{MoS}_2$ , hence significantly improving the HER activity. However, the sulfurization temperature plays an important role in determining the intrinsic structures and sizes of the  $\text{MoO}_2$  core. As shown in Figure 5A, as the sulfurization temperature increases, the HER activity of  $\text{MoS}_2$  samples increases first (from  $200$  to  $300^\circ\text{C}$ ), reaches a

maximum value at 300 °C, and then drops sharply afterward (from 300 to 500 °C). The catalysts obtained at low temperatures generally contain rich defects, which can provide more active sites and are beneficial to the HER activity. Nevertheless, defects are also detrimental to the in-layer conductivity of MoS<sub>2</sub>. Therefore, a balance between active sites and conductivity is necessary to obtain an optimal condition. As temperature increases, the crystallinity of the catalysts is generally improved, inferring less defects and better conductivity. As a result, the activity is enhanced gradually by increasing temperature from 200 to 300 °C but decreases at higher temperature.

The Tafel slope, the inherent property of an electrocatalyst, can be determined by the rate-limiting step of HER. In Figure S8B, the Tafel slope was calculated from the linear portion of the Tafel plots by fitting the experimental data to the Tafel equation of  $\eta = b \log j + a$ , where  $j$  is the current density and  $b$  is the Tafel slope. The Tafel slope was estimated to be 86.4 mV/dec, 35.6 mV/dec, and 101.8 mV/dec for MoO<sub>3</sub>, 3D MoS<sub>2</sub>/MoO<sub>2</sub> (at 300 °C), and MoS<sub>2</sub>, respectively. It should be noted that in an acidic medium, three principal steps have been proposed for the conversion of H<sup>+</sup> to H<sub>2</sub>, commonly referred to as the Volmer, Heyrovsky, and Tafel reactions with the corresponding Tafel slopes of 120, 40, and 30 mV/dec, respectively.<sup>S1,S2</sup> The Tafel slope of 35.6 mV/dec for MoS<sub>2</sub>/MoO<sub>2</sub> suggests that the HER mechanism proceeds through the Heyrovsky-Tafel reaction. The exchange current density ( $j_0$ ) is another important HER parameter, which is the intrinsic property of a catalyst to split a water molecule into hydrogen atoms without any external potential. The exchange current densities for MoO<sub>3</sub>, 3D MoS<sub>2</sub>/MoO<sub>2</sub>, and MoS<sub>2</sub> were determined by extrapolating the Tafel plot as shown in Figure S8. The exchange current density for 3D MoS<sub>2</sub>/MoO<sub>2</sub> was determined to be  $9.0 \times 10^{-4}$  mA cm<sup>-2</sup>, which is remarkably higher than those of MoO<sub>3</sub> ( $1.69 \times 10^{-7}$  mA cm<sup>-2</sup>) and MoS<sub>2</sub> ( $5.4 \times 10^{-7}$  mA cm<sup>-2</sup>). To further confirm the role of underlying MoO<sub>3</sub> cores and the enhancing effect of amorphous MoS<sub>2</sub> on the HER activity of 3D MoS<sub>2</sub>/MoO<sub>2</sub>, samples were synthesized by increasing the sulfurization time from 30 min to 2 h at the same temperature of 300 °C. The HER activities of the as-prepared samples were compared in terms of current density and Tafel slope as shown in Figures S9, A–B. The HER activity decreases sharply with the increasing sulfurization time, which gives a strong evidence that the enhanced HER activity in 3D MoS<sub>2</sub>/MoO<sub>2</sub> stems from the conductive underlying MoO<sub>3</sub>. We further applied Raman spectroscopy (Figure S9 C) to confirm that the size of the underlying MoO<sub>3</sub> decreases as the sulfurization time increases and all MoO<sub>3</sub> converted completely to MoS<sub>2</sub> after 2 h sulfurization. These results clearly indicate that MoO<sub>3</sub> plays a crucial role in the HER reaction.

The electrochemical impedance spectroscopy (EIS) is an effective technique to investigate the interface reactions and electrode kinetics of the catalysts in HER. Figure 5C shows the representative Nyquist plots of the MoO<sub>3</sub>, 3D MoS<sub>2</sub>/MoO<sub>2</sub>, and MoS<sub>2</sub> electrodes. More detailed analyses were carried out by fitting the impedance data to an equivalent circuit (as depicted in the inset of Figure 5C), where a constant phase element (CPE) was employed. The Nyquist plots reveal a remarkable decrease of the charge-transfer resistance ( $R_{CT}$ ) from 2.90 Ω (MoS<sub>2</sub>) to 0.14 Ω (3D MoS<sub>2</sub>/MoO<sub>2</sub>), suggesting that the highly conductive MoO<sub>3</sub> substrates could effectively reduce the resistance of the composite catalysts of 3D MoS<sub>2</sub>/

MoO<sub>3</sub>. Moreover, the series resistance ( $R_s$ ) decreased from 5.35 Ω of MoS<sub>2</sub> to 1.42 Ω of 3D MoS<sub>2</sub>/MoO<sub>3</sub>. The electrochemical double-layer capacitances ( $C_{dl}$ ) were also measured to evaluate the effective surface area of various catalysts. The 3D MoS<sub>2</sub>/MoO<sub>3</sub> exhibited a much larger  $C_{dl}$  of 37.7 μF than the other counterparts, indicating the high exposure of effective active sites. As a consequence, 3D MoS<sub>2</sub>/MoO<sub>3</sub> possesses rich effective active sites and high overall conductivity, leading to the superior HER activity.

Besides the HER activity, the stability is another important criterion to evaluate an HER electrocatalyst. To study the stability in acidic environment, the long-term potential cycling stability of 3D MoS<sub>2</sub>/MoO<sub>3</sub> was tested by taking a potential scan from -0.4 to 0.1 V for 1000 cycles with an accelerated scanning rate of 100 mV s<sup>-1</sup>. As depicted in Figure 5D, there is only a slight activity loss after 1000 cycles, manifesting a good durability, consistent with the previous report of a MoS<sub>2</sub>-based electrocatalyst. The slight loss of HER activity (Figure 5D) after 1000 cycles may result from the H<sup>+</sup> consumption in the electrolyte, or the remaining H<sub>2</sub> bubbles on the electrode surface, which partially hinders the HER process. From our experiments, this decrease of HER activity can be eliminated by refreshing electrolyte and thoroughly releasing the H<sub>2</sub> bubbles on the electrode. As shown in the inset of Figure 5D, the current density decreased slightly even after 1000 cycles, clearly indicating the superior stability. To further probe the stability of 3D MoS<sub>2</sub>/MoO<sub>3</sub> in acidic environment, a continuous HER process was performed at -0.2 V (vs HER). The time-dependent current response for the 3D MoS<sub>2</sub>/MoO<sub>3</sub> was measured as presented in the inset of Figure 5D. From the  $i-t$  curve, it can be seen that a negligible loss in current density was measured after the continuous operation for 3000 s. As tabulated in Table S4, the remarkable performance metrics of 3D MoS<sub>2</sub>/MoO<sub>3</sub> in HER are compared with other previously reported MoS<sub>2</sub>-based electrocatalysts. Additionally, the data before and after the  $iR$  correction are also provided for comparison in Figure S10.

## 4. CONCLUSION

In this study, we have developed distorted MoS<sub>2</sub> nanosheets on a 3D MoO<sub>3</sub> metallic core by a two-step CVD process. Such a novel hybrid structure acts as an active catalyst effectively in HER and exhibits an excellent long-term stability with a small overpotential of ~0.1 V, large cathodic current density (85 mA cm<sup>-2</sup> at  $\eta$  = 300 mV), and small Tafel slope of 35.6 mV/dec. The metallic 3D MoO<sub>3</sub> core, formed by the partial reduction of MoO<sub>3</sub>, serves as a highly conductive layer, which facilitates the fast charge transport and collection; meanwhile, the distorted MoS<sub>2</sub> nanosheets play the role of an HER catalyst with tremendous amount of exposed active sites and also protect the inner MoO<sub>3</sub> core from an acidic electrolyte. The excellent electrocatalytic performance of 3D MoS<sub>2</sub>/MoO<sub>3</sub> potentially enables this hybrid structure to replace the high-cost Pt catalyst.

## ■ ASSOCIATED CONTENT

### Supporting Information

The Supporting Information is available free of charge on the ACS Publications website at DOI: 10.1021/acsami.5b07960.

Figures S1–S10 (EDX, TEM, SEM, XPS, and detailed electrochemical analysis) and Tables S1–S4 (observed Raman scattering bands, analyses from XPS spectra, and comparison of HER performances (PDF)



## AUTHOR INFORMATION

### Corresponding Authors

\*E-mail: lance.li@kaust.edu.sa.

\*E-mail: ytcchem@ntu.edu.tw.

### Author Contributions

@R.D.N. and A.-Y.L. contributed equally.

### Notes

The authors declare no competing financial interest.

## ACKNOWLEDGMENTS

This work was partially supported by the Ministry of Science and Technology (MOST) of Taiwan under MOST 103-2627-M-002-009 and 103-2113-M-002-014-MY3.

## REFERENCES

- (1) Dresselhaus, M. S.; Thomas, I. L. Alternative Energy Technologies. *Nature* **2001**, *414*, 332–337.
- (2) Chu, S.; Majumdar, A. Opportunities and Challenges for a Sustainable Energy Future. *Nature* **2012**, *488*, 294–303.
- (3) Turner, J. A. Sustainable Hydrogen Production. *Science* **2004**, *305*, 972–974.
- (4) Paracchino, A.; Laporte, V.; Sivula, K.; Grätzel, M.; Thimsen, E. Highly Active Oxide Photocathode for Photoelectrochemical Water Reduction. *Nat. Mater.* **2011**, *10*, 456–461.
- (5) Hou, Y.; Abrams, B. L.; Vesborg, P. C. K.; Björketun, M. E.; Herbst, K.; Bech, L.; Setti, A. M.; Damsgaard, C. D.; Pedersen, T.; Hansen, O.; Rossmeisl, J.; Dahl, S.; Nørskov, J. K.; Chorkendorff, I. Bioinspired Molecular co-Catalysts Bonded to a Silicon Photocathode for Solar Hydrogen Evolution. *Nat. Mater.* **2011**, *10*, 434–438.
- (6) Desmond Ng, J. W.; Gorlin, Y.; Hatsukade, T.; Jaramillo, T. F. A Precious-Metal-Free Regenerative Fuel Cell for Storing Renewable Electricity. *Adv. Energy Mater.* **2013**, *3*, 1545–1550.
- (7) Benck, J. D.; Lee, S. C.; Fong, K. D.; Kibsgaard, J.; Sinclair, R.; Jaramillo, T. F. Designing Active and Stable Silicon Photocathodes for Solar Hydrogen Production Using Molybdenum Sulfide Nanomaterials. *Adv. Energy Mater.* **2014**, *4*, 1400739.
- (8) Li, Y.; Wang, H.; Xie, L.; Liang, Y.; Hong, G.; Dai, H. MoS<sub>2</sub> Nanoparticles Grown on Graphene: An Advanced Catalyst for the Hydrogen Evolution Reaction. *J. Am. Chem. Soc.* **2011**, *133*, 7296–7299.
- (9) Lin, J.; Peng, Z.; Wang, G.; Zakhidov, D.; Larios, E.; Yacamán, M. J.; Tour, J. M. Enhanced Electrocatalysis for Hydrogen Evolution Reactions from WS<sub>2</sub> Nanoribbons. *Adv. Energy Mater.* **2014**, *4*, 1301875.
- (10) Wang, D.-Y.; Gong, M.; Chou, H.-L.; Pan, C.-J.; Chen, H.-A.; Wu, Y.; Lin, M.-C.; Guan, M.; Yang, J.; Chen, C.-W.; Wang, Y.-L.; Hwang, B.-J.; Chen, C.-C.; Dai, H. Highly Active and Stable Hybrid Catalyst of Cobalt-Doped FeS<sub>2</sub> Nanosheets–Carbon Nanotubes for Hydrogen Evolution Reaction. *J. Am. Chem. Soc.* **2015**, *137*, 1587–1592.
- (11) Wang, H.; Kong, D.; Johanes, P.; Cha, J. J.; Zheng, G.; Yan, K.; Liu, N.; Cui, Y. MoSe<sub>2</sub> and WSe<sub>2</sub> Nanofilms with Vertically Aligned Molecular Layers on Curved and Rough Surfaces. *Nano Lett.* **2013**, *13*, 3426–3433.
- (12) Zhang, H.; Yang, B.; Wu, X.; Li, Z.; Lei, L.; Zhang, X. Polymorphic CoSe<sub>2</sub> with Mixed Orthorhombic and Cubic Phases for Highly Efficient Hydrogen Evolution Reaction. *ACS Appl. Mater. Interfaces* **2015**, *7*, 1772–1779.
- (13) Jaramillo, T. F.; Jorgensen, K. P.; Bonde, J.; Nielsen, J. H.; Horch, S.; Chorkendorff, I. Identification of Active Edge Sites for Electrochemical H<sub>2</sub> Evolution from MoS<sub>2</sub> Nanocatalysts. *Science* **2007**, *317*, 100–102.
- (14) Lassalle-Kaiser, B.; Merki, D.; Vrubel, H.; Gul, S.; Yachandra, V. K.; Hu, X.; Yano, J. Evidence from in Situ X-ray Absorption Spectroscopy for the Involvement of Terminal Disulfide in the Reduction of Protons by an Amorphous Molybdenum Sulfide Electrocatalyst. *J. Am. Chem. Soc.* **2015**, *137*, 314–321.
- (15) Laursen, A. B.; Kegnaes, S.; Dahl, S.; Chorkendorff, I. Molybdenum Sulfides-Efficient and Viable Materials for Electro- and Photoelectrocatalytic Hydrogen Evolution. *Energy Environ. Sci.* **2012**, *5*, 5577–5591.
- (16) Hu, S. Y.; Liang, C. H.; Tiong, K. K.; Lee, Y. C.; Huang, Y. S. Preparation and Characterization of Large Niobium-Doped MoSe<sub>2</sub> Single Crystals. *J. Cryst. Growth* **2005**, *285*, 408–414.
- (17) Kong, D.; Wang, H.; Cha, J. J.; Pasta, M.; Koski, K. J.; Yao, J.; Cui, Y. Synthesis of MoS<sub>2</sub> and MoSe<sub>2</sub> Films with Vertically Aligned Layers. *Nano Lett.* **2013**, *13*, 1341–1347.
- (18) Liao, L.; Zhu, J.; Bian, X.; Zhu, L.; Scanlon, M. D.; Girault, H. H.; Liu, B. MoS<sub>2</sub> Formed on Mesoporous Graphene as a Highly Active Catalyst for Hydrogen Evolution. *Adv. Funct. Mater.* **2013**, *23*, 5326–5333.
- (19) Hou, Y.; Zhang, B.; Wen, Z.; Cui, S.; Guo, X.; He, Z.; Chen, J. A 3D Hybrid of Layered MoS<sub>2</sub>/Nitrogen-Doped Graphene Nanosheet Aerogels: An Effective Catalyst for Hydrogen Evolution in Microbial Electrolysis Cells. *J. Mater. Chem. A* **2014**, *2*, 13795–13800.
- (20) Yuan, H.; Li, J.; Yuan, C.; He, Z. Facile Synthesis of MoS<sub>2</sub>@CNT as an Effective Catalyst for Hydrogen Production in Microbial Electrolysis Cells. *ChemElectroChem* **2014**, *1*, 1828–1833.
- (21) Yan, Y.; Ge, X.; Liu, Z.; Wang, J.-Y.; Lee, J.-M.; Wang, X. Facile Synthesis of Low Crystalline MoS<sub>2</sub> Nanosheet-Coated CNTs for Enhanced Hydrogen Evolution Reaction. *Nanoscale* **2013**, *5*, 7768–7771.
- (22) Guo, X.; Cao, G.-L.; Ding, F.; Li, X.; Zhen, S.; Xue, Y.-f.; Yan, Y.-m.; Liu, T.; Sun, K.-n. A Bulky and Flexible Electrocatalyst for Efficient Hydrogen Evolution Based on the Growth of MoS<sub>2</sub> Nanoparticles on Carbon Nanofiber Foam. *J. Mater. Chem. A* **2015**, *3*, 5041–5046.
- (23) Yan, Y.; Xia, B.; Li, N.; Xu, Z.; Fisher, A.; Wang, X. Vertically Oriented MoS<sub>2</sub> and WS<sub>2</sub> Nanosheets Directly Grown on Carbon Cloth as Efficient and Stable 3-Dimensional Hydrogen-Evolving Cathodes. *J. Mater. Chem. A* **2015**, *3*, 131–135.
- (24) Zhou, W.; Zhou, K.; Hou, D.; Liu, X.; Li, G.; Sang, Y.; Liu, H.; Li, L.; Chen, S. Three-Dimensional Hierarchical Frameworks Based on MoS<sub>2</sub> Nanosheets Self-Assembled on Graphene Oxide for Efficient Electrocatalytic Hydrogen Evolution. *ACS Appl. Mater. Interfaces* **2014**, *6*, 21534–21540.
- (25) Chang, Y.-H.; Lin, C.-T.; Chen, T.-Y.; Hsu, C.-L.; Lee, Y.-H.; Zhang, W.; Wei, K.-H.; Li, L.-J. Highly Efficient Electrocatalytic Hydrogen Production by MoS<sub>x</sub> Grown on Graphene-Protected 3D Ni Foams. *Adv. Mater.* **2013**, *25*, 756–760.
- (26) Geng, X.; Wu, W.; Li, N.; Sun, W.; Armstrong, J.; Al-hilo, A.; Brozak, M.; Cui, J.; Chen, T.-p. Three-Dimensional Structures of MoS<sub>2</sub> Nanosheets with Ultrahigh Hydrogen Evolution Reaction in Water Reduction. *Adv. Funct. Mater.* **2014**, *24*, 6123–6129.
- (27) Lukowski, M. A.; Daniel, A. S.; Meng, F.; Forticaux, A.; Li, L.; Jin, S. Enhanced Hydrogen Evolution Catalysis from Chemically Exfoliated Metallic MoS<sub>2</sub> Nanosheets. *J. Am. Chem. Soc.* **2013**, *135*, 10274–10277.
- (28) Voiry, D.; Salehi, M.; Silva, R.; Fujita, T.; Chen, M.; Asefa, T.; Shenoy, V. B.; Eda, G.; Chhowalla, M. Conducting MoS<sub>2</sub> Nanosheets as Catalysts for Hydrogen Evolution Reaction. *Nano Lett.* **2013**, *13*, 6222–6227.
- (29) Shin, S.; Jin, Z.; Kwon, D. H.; Bose, R.; Min, Y.-S. High Turnover Frequency of Hydrogen Evolution Reaction on Amorphous MoS<sub>2</sub> Thin Film Directly Grown by Atomic Layer Deposition. *Langmuir* **2015**, *31*, 1196–1202.
- (30) Zhao, X.; Zhu, H.; Yang, X. Amorphous Carbon Supported MoS<sub>2</sub> Nanosheets as Effective Catalysts for Electrocatalytic Hydrogen Evolution. *Nanoscale* **2014**, *6*, 10680–10685.
- (31) Merki, D.; Fierro, S.; Vrubel, H.; Hu, X. Amorphous Molybdenum Sulfide Films as Catalysts for Electrochemical Hydrogen Production in Water. *Chem. Sci.* **2011**, *2*, 1262–1267.
- (32) Tao, L.; Duan, X.; Wang, C.; Duan, X.; Wang, S. Plasma-Engineered MoS<sub>2</sub> Thin-Film as an Efficient Electrocatalyst for Hydrogen Evolution Reaction. *Chem. Commun.* **2015**, *51*, 7470–7473.
- (33) Xie, J.; Zhang, J.; Li, S.; Grote, F.; Zhang, X.; Zhang, H.; Wang, R.; Lei, Y.; Pan, B.; Xie, Y. Controllable Disorder Engineering in

Oxygen-Incorporated MoS<sub>2</sub> Ultrathin Nanosheets for Efficient Hydrogen Evolution. *J. Am. Chem. Soc.* **2013**, *135*, 17881–17888.

(34) Xie, J.; Zhang, H.; Li, S.; Wang, R.; Sun, X.; Zhou, M.; Zhou, J.; Lou, X. W.; Xie, Y. Defect-Rich MoS<sub>2</sub> Ultrathin Nanosheets with Additional Active Edge Sites for Enhanced Electrocatalytic Hydrogen Evolution. *Adv. Mater.* **2013**, *25*, 5807–5813.

(35) Chen, Z.; Cummins, D.; Reinecke, B. N.; Clark, E.; Sunkara, M. K.; Jaramillo, T. F. Core-shell MoO<sub>3</sub>–MoS<sub>2</sub> Nanowires for Hydrogen Evolution: A Functional Design for Electrocatalytic Materials. *Nano Lett.* **2011**, *11*, 4168–4175.

(36) Tan, Y.; Liu, P.; Chen, L.; Cong, W.; Ito, Y.; Han, J.; Guo, X.; Tang, Z.; Fujita, T.; Hirata, A.; Chen, M. W. Monolayer MoS<sub>2</sub> Films Supported by 3D Nanoporous Metals for High-Efficiency Electrocatalytic Hydrogen Production. *Adv. Mater.* **2014**, *26*, 8023–8028.

(37) Yang, L.; Zhou, W.; Hou, D.; Zhou, K.; Li, G.; Tang, Z.; Li, L.; Chen, S. Porous Metallic MoO<sub>2</sub>-Supported MoS<sub>2</sub> Nanosheets for Enhanced Electrocatalytic Activity in the Hydrogen Evolution Reaction. *Nanoscale* **2015**, *7*, 5203–5208.

(38) Zhou, W.; Hou, D.; Sang, Y.; Yao, S.; Zhou, J.; Li, G.; Li, L.; Liu, H.; Chen, S. MoO<sub>2</sub> Nanobelts@Nitrogen Self-doped MoS<sub>2</sub> Nanosheets as Effective Electrocatalysts for Hydrogen Evolution Reaction. *J. Mater. Chem. A* **2014**, *2*, 11358–11364.

(39) Chang, Y.-H.; Nikam, R. D.; Lin, C.-T.; Huang, J.-K.; Tseng, C.-C.; Hsu, C.-L.; Cheng, C.-C.; Su, C.-Y.; Li, L.-J.; Chua, D. H. C. Enhanced Electrocatalytic Activity of MoS<sub>x</sub> on TCNQ-Treated Electrode for Hydrogen Evolution Reaction. *ACS Appl. Mater. Interfaces* **2014**, *6*, 17679–17685.

(40) Zhang, L.; Wu, H. B.; Yan, Y.; Wang, X.; Lou, X. W. Hierarchical MoS<sub>2</sub> Microboxes Constructed by Nanosheets with Enhanced Electrochemical Properties for Lithium Storage and Water Splitting. *Energy Environ. Sci.* **2014**, *7*, 3302–3306.

(41) Yu, X.-Y.; Hu, H.; Wang, Y.; Chen, H.; Lou, X. W. Ultrathin MoS<sub>2</sub> Nanosheets Supported on N-doped Carbon Nanoboxes with Enhanced Lithium Storage and Electrocatalytic Properties. *Angew. Chem., Int. Ed.* **2015**, *54*, 7395–7398.

(42) Dieterle, M.; Weinberg, G.; Mestl, G. Raman Spectroscopy of Molybdenum Oxides Part I. Structural Characterization of Oxygen Defects in MoO<sub>3-x</sub> by DR UV/VIS, Raman Spectroscopy and X-Ray Diffraction. *Phys. Chem. Chem. Phys.* **2002**, *4*, 812–821.

(43) Lee, Y.-H.; Zhang, X.-Q.; Zhang, W.; Chang, M.-T.; Lin, C.-T.; Chang, K.-D.; Yu, Y.-C.; Wang, J. T.-W.; Chang, C.-S.; Li, L.-J.; Lin, T.-W. Synthesis of Large-Area MoS<sub>2</sub> Atomic Layers with Chemical Vapor Deposition. *Adv. Mater.* **2012**, *24*, 2320–2325.

(44) Vrubel, H.; Hu, X. Growth and Activation of an Amorphous Molybdenum Sulfide Hydrogen Evolving Catalyst. *ACS Catal.* **2013**, *3*, 2002–2011.

(45) Kibsgaard, J.; Jaramillo, T. F.; Besenbacher, F. Building an Appropriate Active-Site Motif into a Hydrogen-Evolution Catalyst with Thiomolybdate [Mo<sub>3</sub>S<sub>13</sub>]<sup>2-</sup> Clusters. *Nat. Chem.* **2014**, *6*, 248–253.

(46) Schroeder, T.; Zegenhagen, J.; Magg, N.; Immaraporn, B.; Freund, H. J. Formation of a Faceted MoO<sub>2</sub> Epilayer on Mo(112) Studied by XPS, UPS and STM. *Surf. Sci.* **2004**, *552*, 85–97.

(47) Sun, Y.; Hu, X.; Yu, J. C.; Li, Q.; Luo, W.; Yuan, L.; Zhang, W.; Huang, Y. Morphosynthesis of a Hierarchical MoO<sub>2</sub> Nanoarchitecture as a Binder-Free Anode for lithium-Ion Batteries. *Energy Environ. Sci.* **2011**, *4*, 2870–2877.

(48) Yoon, S.; Jung, K.-N.; Jin, C. S.; Shin, K.-H. Synthesis of Nitrided MoO<sub>2</sub> and its Application as Anode Materials for Lithium-Ion Batteries. *J. Alloys Compd.* **2012**, *536*, 179–183.

(49) Smith, A. J.; Chang, Y.-H.; Raidongia, K.; Chen, T.-Y.; Li, L.-J.; Huang, J. Molybdenum Sulfide Supported on Crumpled Graphene Balls for Electrocatalytic Hydrogen Production. *Adv. Energy Mater.* **2014**, *4*, 1400398.

(50) Kibsgaard, J.; Chen, Z.; Reinecke, B. N.; Jaramillo, T. F. Engineering the Surface Structure of MoS<sub>2</sub> to Preferentially Expose Active Edge Sites for Electrocatalysis. *Nat. Mater.* **2012**, *11*, 963–969.

(51) Durst, J.; Siebel, A.; Simon, C.; Hasche, F.; Herranz, J.; Gasteiger, H. A. New Insights into the Electrochemical Hydrogen

Oxidation and Evolution Reaction Mechanism. *Energy Environ. Sci.* **2014**, *7*, 2255–2260.

(52) Zheng, Y.; Jiao, Y.; Zhu, Y.; Li, L. H.; Han, Y.; Chen, Y.; Du, A.; Jaroniec, M.; Qiao, S. Z. Hydrogen Evolution by a Metal-Free Electrocatalyst. *Nat. Commun.* **2014**, *5*, 3783.



## Supporting Information

### Three-Dimensional Heterostructures of MoS<sub>2</sub> Nanosheets on Conducting MoO<sub>2</sub> as an Efficient Electrocatalyst to Enhance Hydrogen Evolution Reaction

*Revannath Dnyandeo Nikam,<sup>1,2,3,#</sup> Ang-Yu Lu,<sup>4,#</sup> Poonam Ashok Sonawane,<sup>5,6</sup> U. Rajesh Kumar,<sup>1,2,3</sup> Kanchan Yadav,<sup>1,2,3</sup> Lain-Jong Li,<sup>4,\*</sup> and Yit-Tsong Chen<sup>1,2,\*</sup>*

<sup>1</sup>Department of Chemistry, National Taiwan University, Taipei 106, Taiwan

<sup>2</sup>Institute of Atomic and Molecular Sciences, Academia Sinica, Taipei 106, Taiwan

<sup>3</sup>Nanoscience and Technology Program, Taiwan International Graduate Program, Academia Sinica, Taipei 115, Taiwan

<sup>4</sup>Division of Physical Science & Engineering, King Abdullah University of Science and Technology Thuwal 23955-6900, Kingdom of Saudi Arabia

<sup>5</sup>Institute of Chemistry, Academia Sinica, Taipei 115, Taiwan

<sup>6</sup>Department of Applied Chemistry, National Chiao-Tung University, Hsinchu 300, Taiwan

*\* Address correspondence to: lance.li@kaust.edu.sa, ytcchem@ntu.edu.tw*

*# equally contributed*

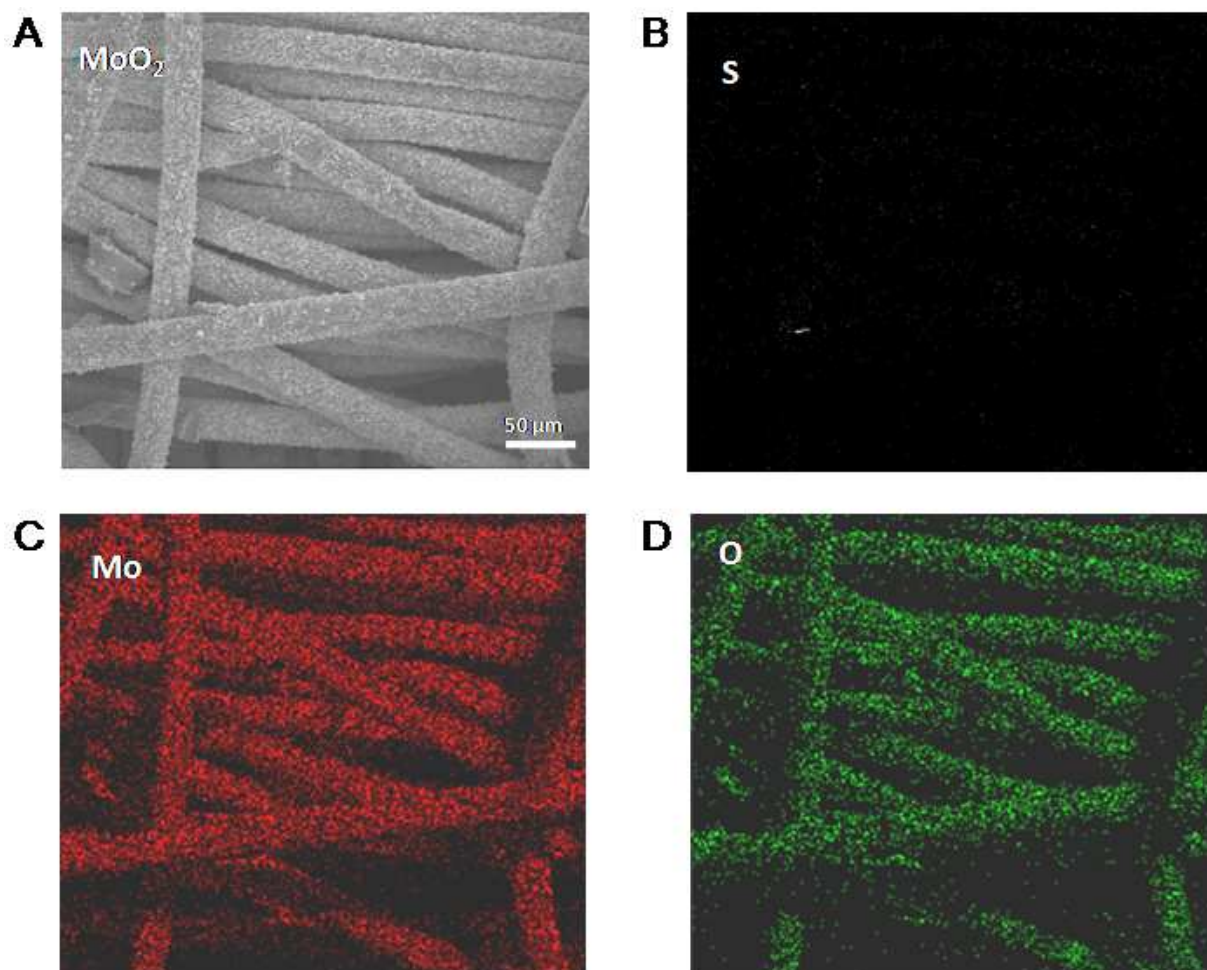


**Figure S1.** EDX elemental mapping images of Mo, S, and O in the unsulfidized  $\text{MoO}_2$ .

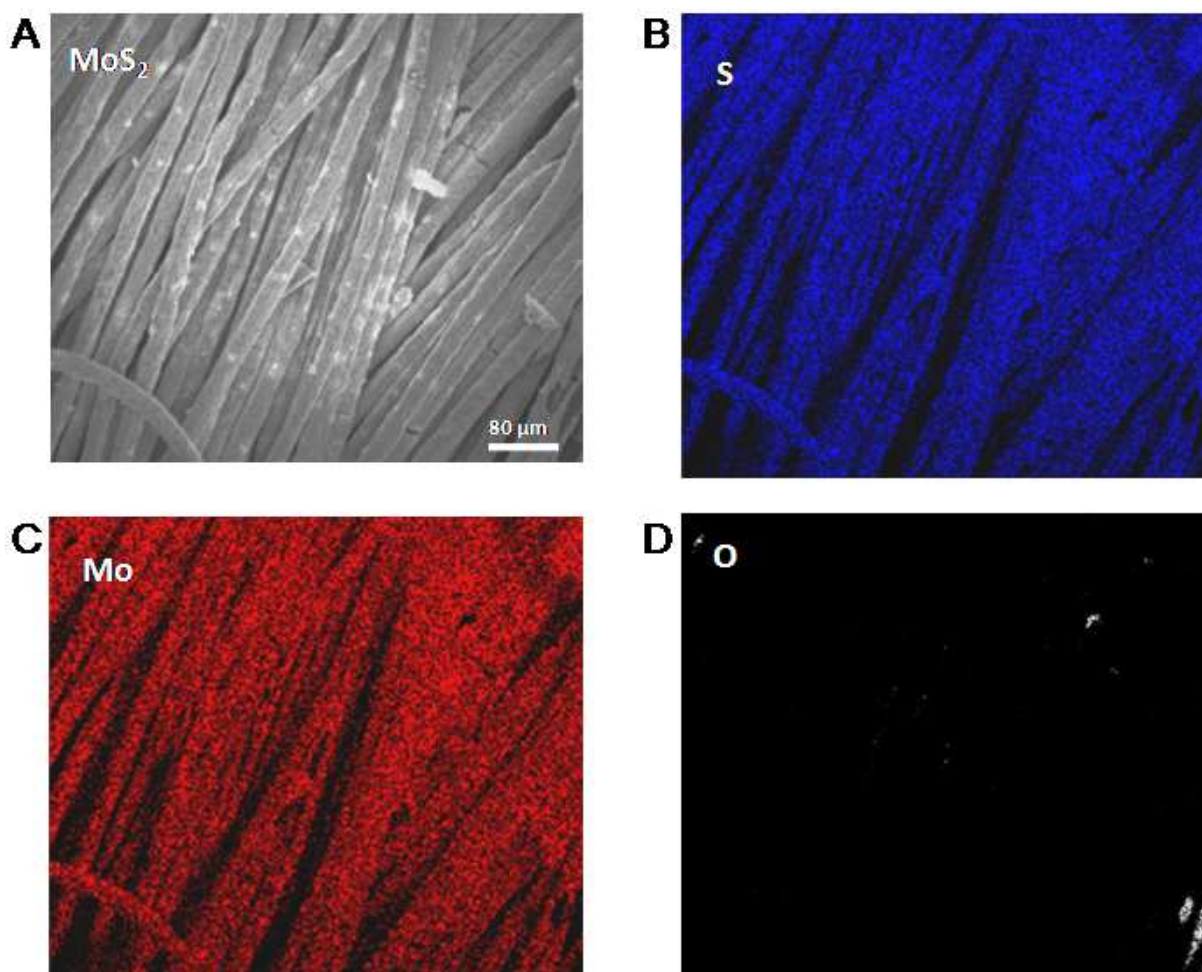


**Figure S2.** EDX elemental mapping images of Mo, S, and O in the MoS<sub>2</sub> nanosheets prepared at 1000 °C.



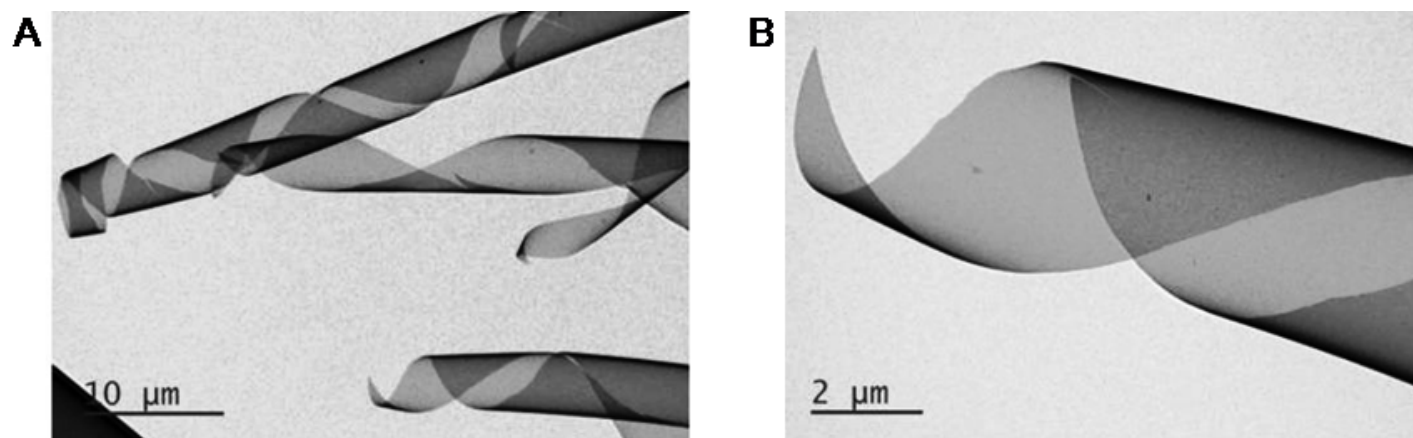


**Figure S3.** (A–B) TEM images of the detached MoO<sub>2</sub> core from a carbon cloth substrate by sonication show the spiral-like morphology of MoO<sub>2</sub> nanosheets.

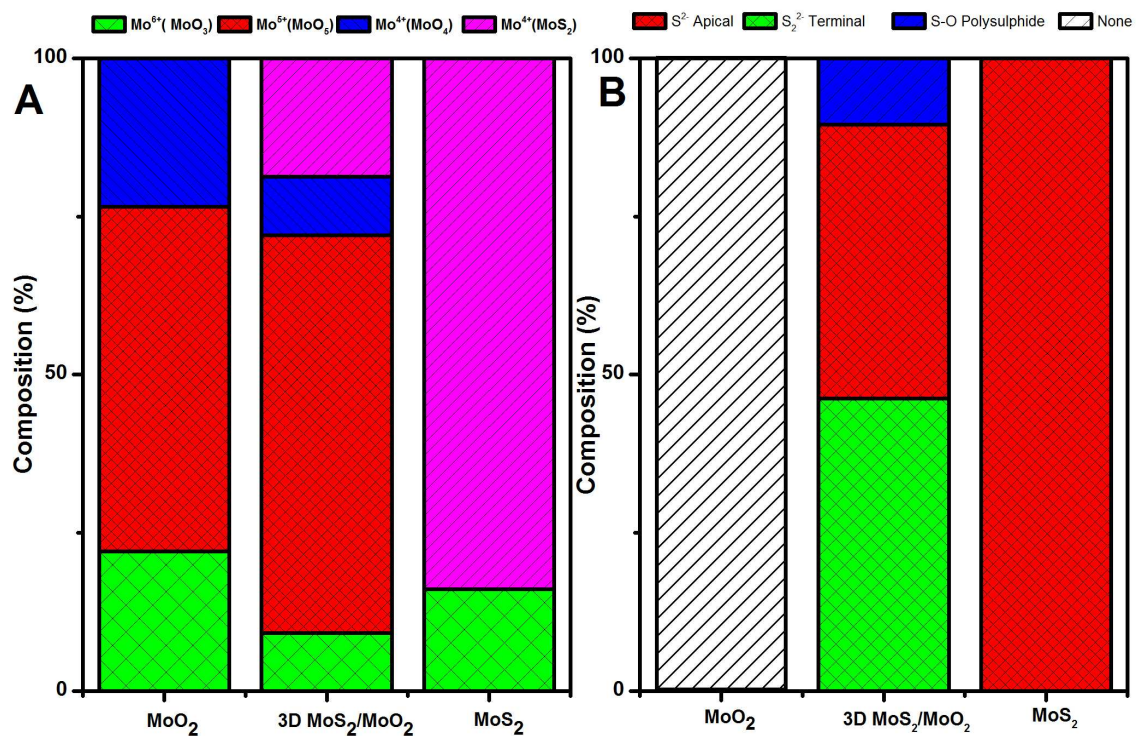


**Figure S4.** Fractional percentage compositions of different specimens calculated from the XPS spectral data of (A) Mo 3d<sub>5/2-3/2</sub> and (B) S 2p<sub>3/2-1/2</sub> for MoO<sub>2</sub>, 3D MoS<sub>2</sub>/MoO<sub>2</sub>, and MoS<sub>2</sub>.

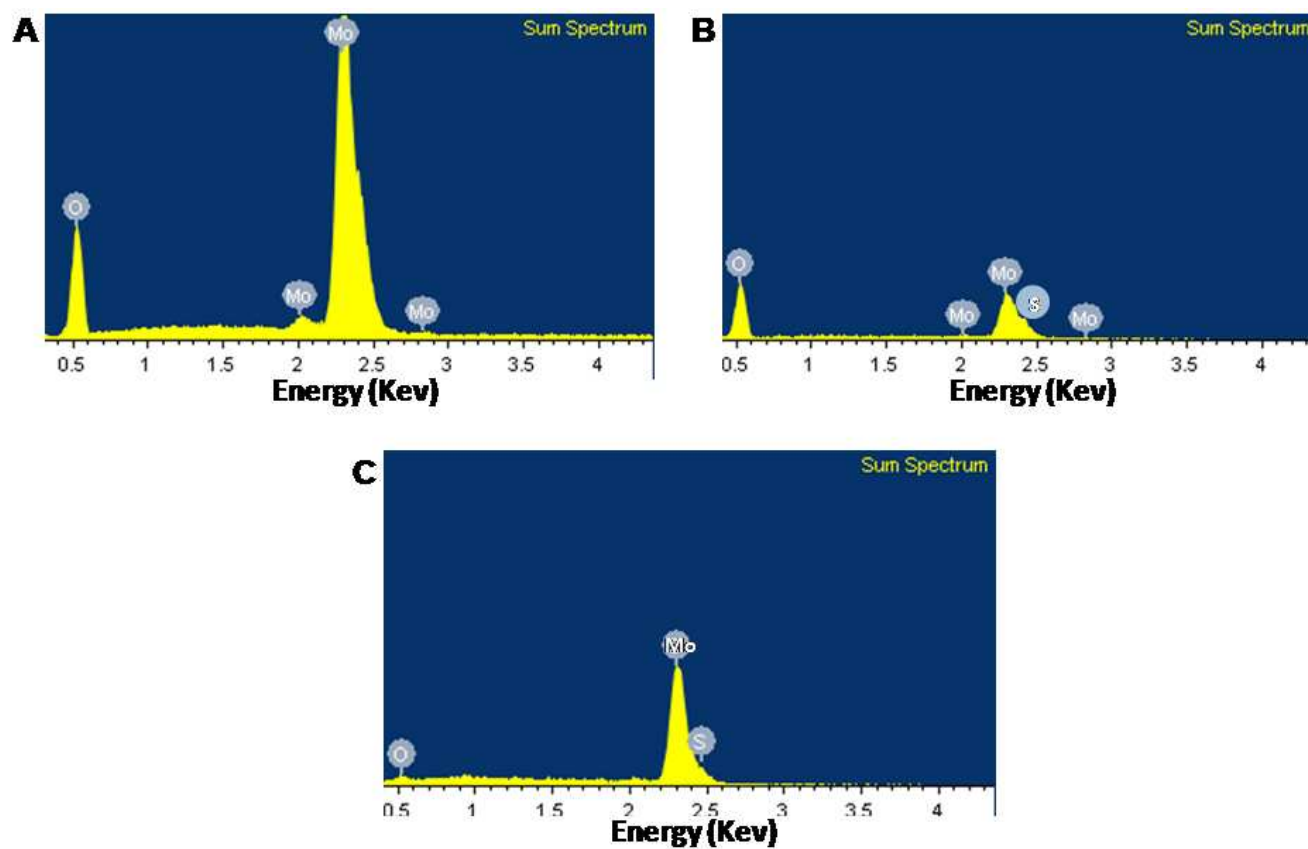


**Figure S5.** Elemental analyses of the (A) MoO<sub>2</sub>, (B) 3D MoS<sub>2</sub>/MoO<sub>2</sub>, and (c) MoS<sub>2</sub> samples by EDX spectroscopy indicate the presence of Mo, O, and S.



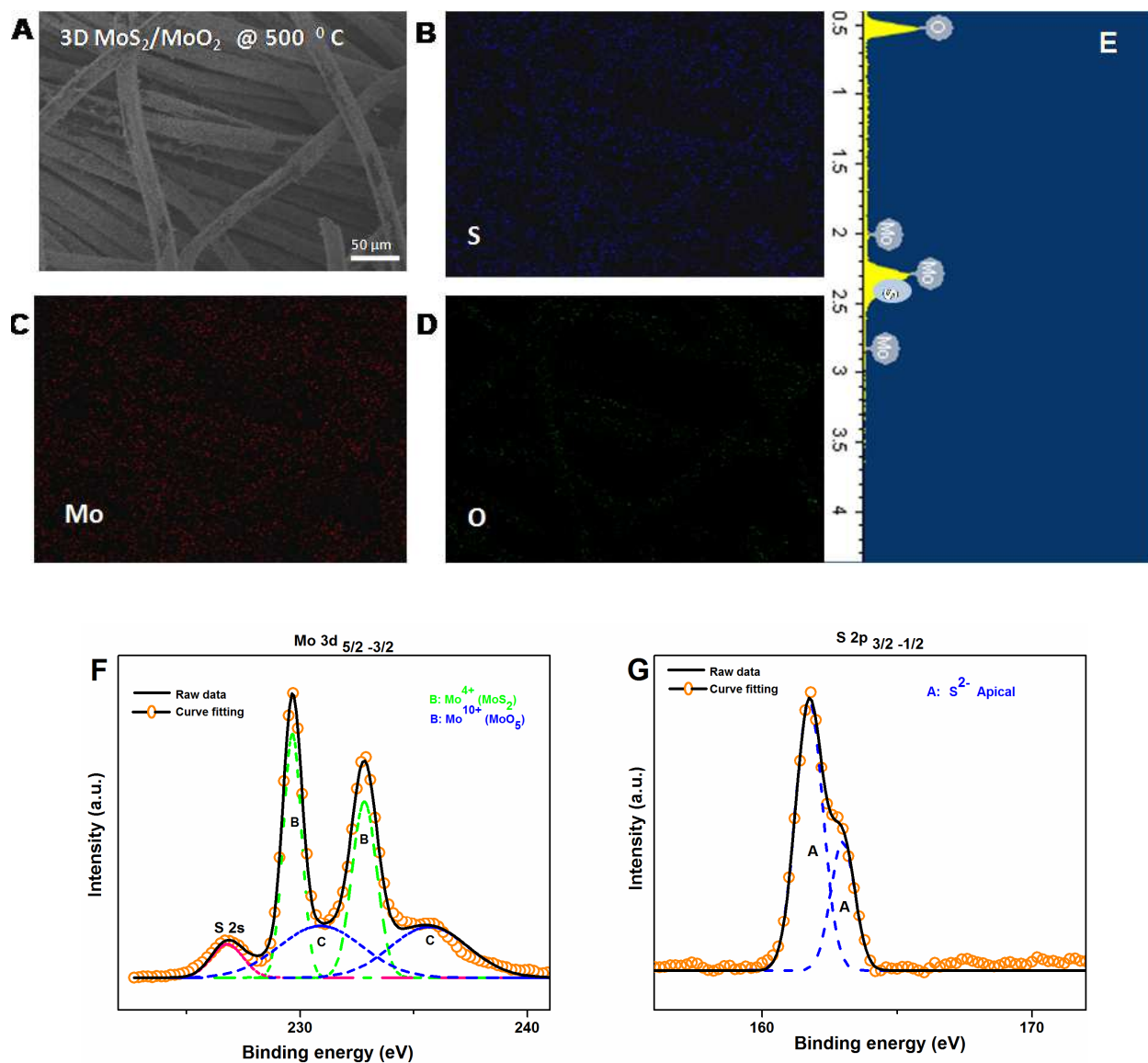


**Figure S6.** Structural and compositional analyses for the 3D MoS<sub>2</sub>/MoO<sub>2</sub> sample prepared at 500 °C. (A) SEM image of the 3D MoS<sub>2</sub>/MoO<sub>2</sub>. (B–D) Selected-area elemental mappings by EDX for (B) S, (C) Mo, and (D) O. (E) Selected-area EDX spectrum of Mo, O, and S. (F) High-resolution XPS spectrum of Mo 3d<sub>5/2-3/2</sub>. (G) High-resolution XPS spectrum of S 2p<sub>3/2-1/2</sub>.

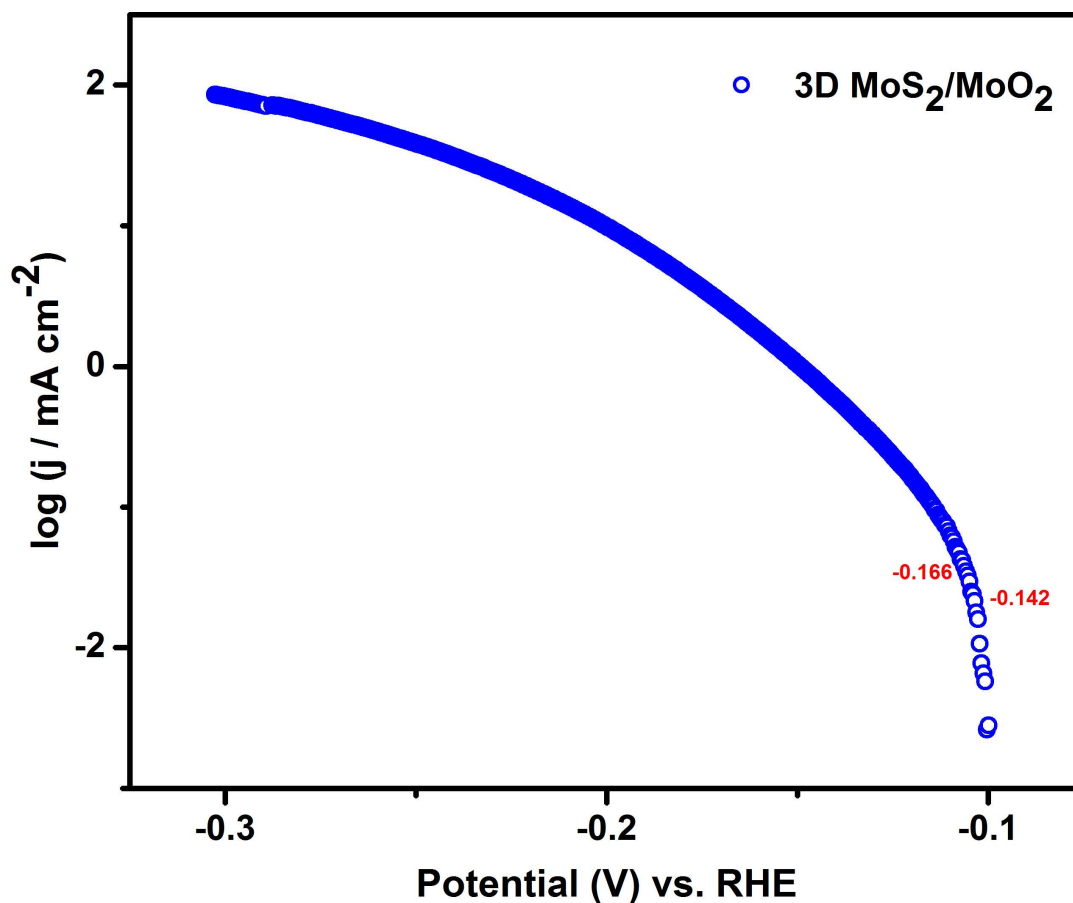


**Figure S7.** Calculation of the onset potential ( $\eta$ ). The Tafel plot of the 3D MoS<sub>2</sub>/MoO<sub>2</sub> recorded in the region of low current densities. The onset potential for HER was determined from the semi-log plot. The semi-log plot of 3D MoS<sub>2</sub>/MoO<sub>2</sub> in the region of low current densities is shown in Figure S8. The linear relationship is below -0.142 V, but starts to deviate above -0.166 V. Therefore, -0.142 V was chosen as the onset potential for 3D MoS<sub>2</sub>/MoO<sub>2</sub>. The same method was applied to determine the onset potentials for other samples.

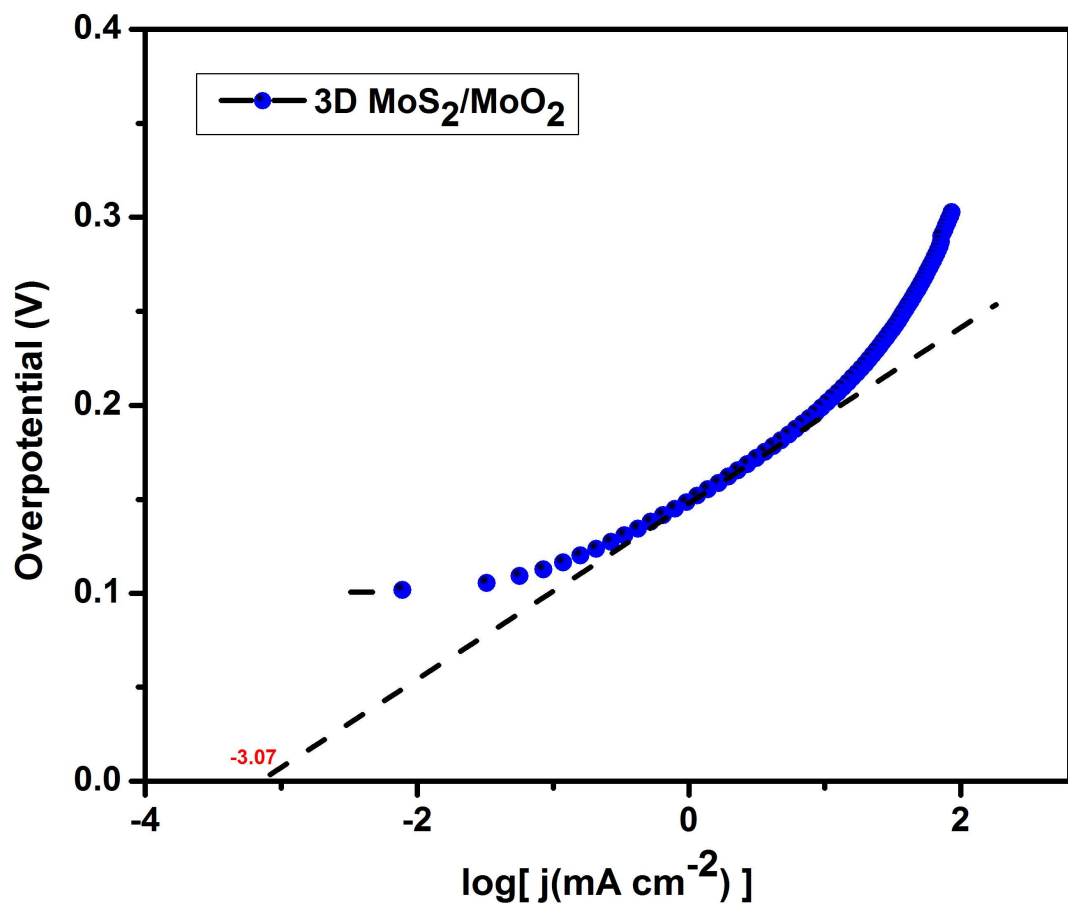


**Figure S8.** Calculation of the exchange current density ( $j_0$ ). Tafel plots were used for calculating the exchange current density ( $j_0$ ) of the 3D MoS<sub>2</sub>/MoO<sub>2</sub> with an extrapolation method. A linear fit of the Tafel plots to zero overpotential gives the value of  $j_0$ . Based on the above calculation, log ( $j$ ) at zero overpotential for 3D MoS<sub>2</sub>/MoO<sub>2</sub> is -3.07 and  $j_0$  was calculated to be  $9.0 \times 10^{-4}$  mA cm<sup>-2</sup>. The same methods were applied to determine the exchange current densities of other samples.



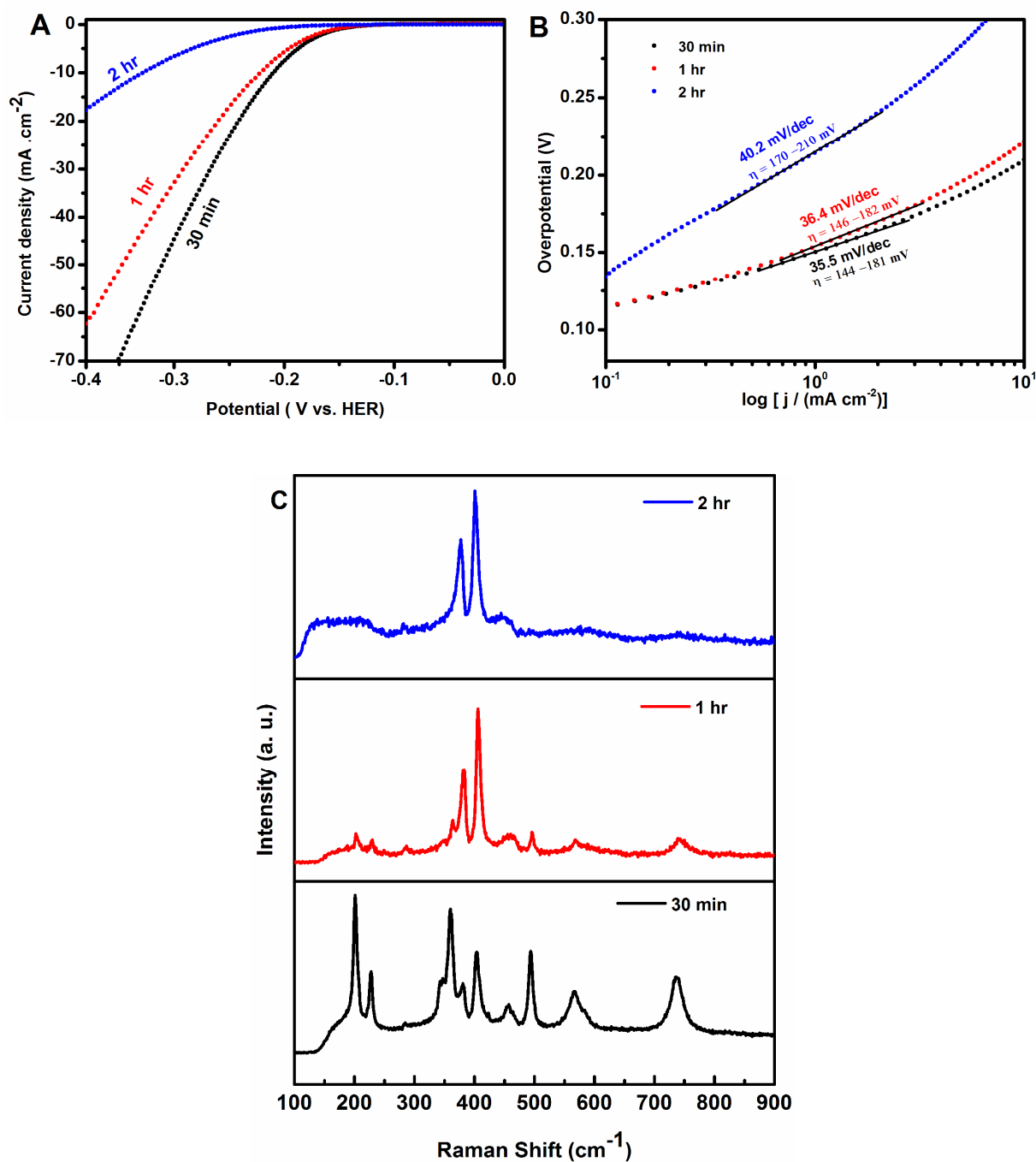


**Figure S9.** The samples were prepared at the same sulfurization temperature (300 °C) but with different sulfurization times of 30 min, 1 hr, and 2 hr, respectively. (A) Polarization curves, (B) Tafel plots, and (C) Raman spectra of the as-obtained samples prepared at various sulfurization times.

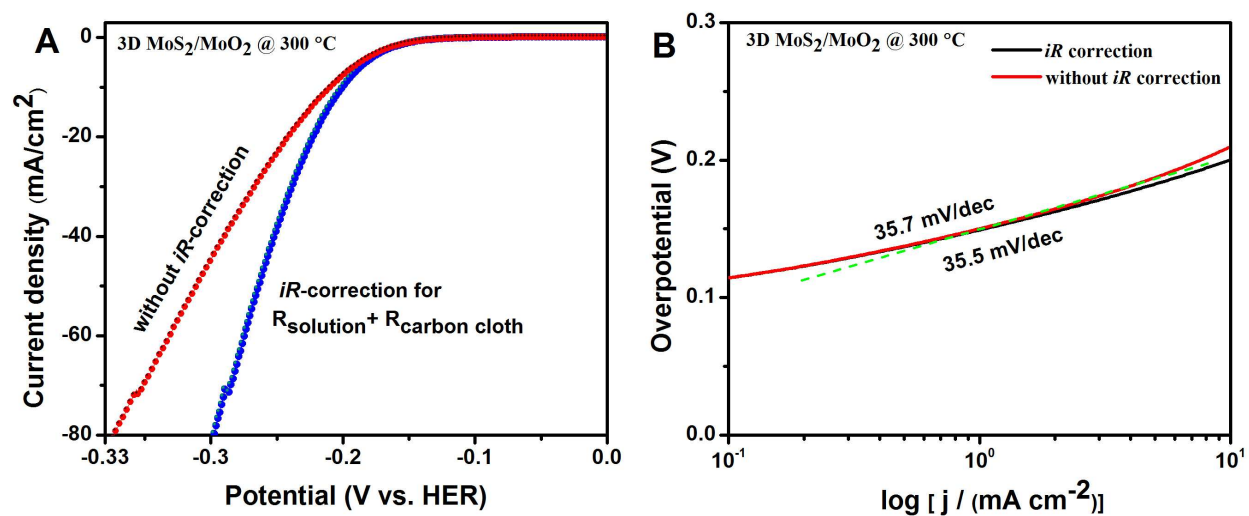


**Figure S10.** (A) The polarization curves with and without the *iR* correction. (B) The Tafel slopes with and without the *iR* correction.

**Table S1.** The observed Raman scattering bands in MoO<sub>2</sub>, 3D MoS<sub>2</sub>/MoO<sub>2</sub>, and MoS<sub>2</sub>

Peak number	Raman shift (cm <sup>-2</sup> )	Mode & assignment	Parent material
1	203	stretching of the Mo-O-Mo bridge	MoO <sub>2</sub>
2	228	stretching of the Mo-O-Mo bridge	MoO <sub>2</sub>
3	286	E <sub>1g</sub> -mode of S atoms in the basal plane	MoS <sub>2</sub>
4	345	antisymmetric stretching of the Mo-O-Mo bridge	MoO <sub>2</sub>
5	363	stretching of the Mo-O-Mo bridge	MoO <sub>2</sub>
6	384	E <sub>2g</sub> -mode of Mo + S atoms in the basal plane	MoS <sub>2</sub>
7	405	A <sub>1g</sub> -mode of S atoms along the c axis	MoS <sub>2</sub>
8	461	B <sub>2g</sub> -antisymmetric stretching of the Mo-O-Mo bridge	MoO <sub>2</sub>
9	495	B <sub>3g</sub> -antisymmetric stretching of the Mo-O-Mo bridge	MoO <sub>2</sub>
10	571	oxygen stretching in O-Mo-O terminal	MoO <sub>2</sub>
11	589	B <sub>1</sub> -mode oxygen stretching in O-Mo-O terminal	MoO <sub>2</sub>
12	741	A <sub>g</sub> -mode oxygen stretching in O-Mo-O terminal	MoO <sub>2</sub>



**Table S2.** Analyses from the XPS spectra in the S 2p region of MoO<sub>2</sub>, 3D MoS<sub>2</sub>/MoO<sub>2</sub>, and MoS<sub>2</sub>

Region		MoO <sub>2</sub>				3D MoS <sub>2</sub> /MoO <sub>2</sub>				MoS <sub>2</sub>			
		Position (eV)	FWHM (eV)	Fraction# (%)	Normalized area	Position (eV)	FWHM (eV)	Fraction# (%)	Normalized area	Position (eV)	FWHM (eV)	Fraction# (%)	Normalized area
S 2p	Apical S <sup>2-</sup> 2p <sub>3/2</sub>	-	-	-	-	162.1	1.42	46.20	379	162.1	0.98	100	1557
	Apical S <sup>2-</sup> 2p <sub>1/2</sub>	-	-		-	163.3	1.42		189	163.3	0.98		1024
	Terminal S <sub>2</sub> <sup>2-</sup> 2p <sub>3/2</sub>	-	-	-	-	163.7	2.01	43.29	445	-	-	-	-
	Terminal S <sub>2</sub> <sup>2-</sup> 2p <sub>1/2</sub>	-	-		-	164.9	2.01		222	-	-		-
	Polysulphide S-O	-	-	-	-	178.1	4.24	10.49	117	-	-	-	-

# Fractional % of S<sup>2-</sup> is calculated from % S<sup>2-</sup> = (the peak area under ( S<sup>2-</sup> 2p<sub>3/2</sub> + S<sup>2-</sup> 2p<sub>1/2</sub> )/the sensitivity factor of S<sup>2-</sup> ) × 100. The same method was applied to calculate the fractional % of S<sub>2</sub><sup>2-</sup> and S-O.

**Table S3.** Analyses from the XPS spectra in the Mo 3d region of MoO<sub>2</sub>, 3D MoS<sub>2</sub>/MoO<sub>2</sub>, and MoS<sub>2</sub>

Region		MoO <sub>2</sub>				3D MoS <sub>2</sub> /MoO <sub>2</sub>				MoS <sub>2</sub>			
		Position (eV)	FWHM (eV)	Fraction# (%)	Normalized area	Position (eV)	FWHM (eV)	Fraction# (%)	Normalized area	Position# (eV)	FWHM (eV)	Fraction (%)	Normalized area
Mo 3d	Mo <sup>+4</sup> 3d <sub>5/2</sub> (MoO <sub>2</sub> )	229.8	0.85	13.62	2598.14	229.8	1	4.74	766.097	-	-	-	-
	Mo <sup>+4</sup> 3d <sub>3/2</sub> (MoO <sub>2</sub> )	233.0	0.85	8.41	1603.80	233.04	1	3.30	533.50	-	-	-	-
	Mo <sup>+10</sup> 3d <sub>5/2</sub> (MoO <sub>5</sub> )	231.9	3.52	42.86	8173.36	231.9	3.9	43.95	7098.87	-	-	-	-
	Mo <sup>+10</sup> 3d <sub>5/2</sub> (MoO <sub>5</sub> )	234.6	3.52	11.19	5448.1	234.6	3.9	17.94	4732.2	-	-	-	-
	Mo <sup>+6</sup> 3d <sub>5/2</sub> (MoO <sub>3</sub> )	235.4	3.04	19.25	3670.28	235.4	4.5	5.04	815.23	235.4	4.6	11.9	1145.50
	Mo <sup>+6</sup> 3d <sub>3/2</sub> (MoO <sub>3</sub> )	238.7	3.04	4.64	3446.2	238.7	4.5	3.27	528.24	238.7	4.6	4.19	763.3
	Mo <sup>+4</sup> 3d <sub>5/2</sub> (MoS <sub>2</sub> )	-	-	-	-	229.6	0.97	14.20	2294.48	229.6	1.14	40.23	3871.32
	Mo <sup>+4</sup> 3d <sub>3/2</sub> (MoS <sub>2</sub> )	-	-	-	-	232.8	0.97	4.10	1529.1	232.8	1.14	28.14	2742.27
	2s (MoS <sub>2</sub> )	-	-	-	-	226.7	2.76	3.41	551.40	226.7	2.27	15.15	1458.27

#Fractional % of Mo<sup>+6</sup> is calculated as % Mo<sup>+6</sup> = (the peak area under (Mo<sup>+6</sup> 3d<sub>5/2</sub> + Mo<sup>+6</sup> 3d<sub>3/2</sub>)/the sensitivity factor of Mo<sup>+6</sup>) × 100. The same method was applied to calculate the fractional % of other element.

**Table S4.** Comparison of HER performances of 3D MoS<sub>2</sub>/MoO<sub>2</sub> and other MoS<sub>2</sub> catalyst

Catalyst	Loading mass (mg/cm <sup>2</sup> )	$\eta$ (mV)	Current density (mAcm <sup>-2</sup> ) at ( $\eta = -0.2$ V)	Tafel slope (mA/dec)	Exchange current density (mAcm <sup>-2</sup> )	Ref.
3D MoS <sub>2</sub> /MoO <sub>2</sub> on carbon cloth *	0.30	-142	-85	35.6	$9.0 \times 10^{-4}$	This work
MoS <sub>2</sub> nanoparticale on Au (111)	-	-150	-0.67	55–60	$1.3 \times 10^{-4}$	<i>Science</i> , <b>2007</b> , 317, 100
MoO <sub>3</sub> -MoS <sub>2</sub> on FTO *	-	-150	-10	50–60	$8.2 \times 10^{-4}$	<i>Nano Lett.</i> <b>2011</b> , 11, 4168
1T MoS <sub>2</sub> on graphite *	-	-187	-10	43	-	<i>JACS</i> , <b>2013</b> , 135, 10274.
Monolayer MoS <sub>2</sub> on 3D nanoporous gold	-	-118	-1.5	46	$6.9 \times 10^{-4}$	<i>Adv. Mater.</i> , <b>2014</b> , 26, 8023
double-gyroid MoS <sub>2</sub> on FTO *	0.06	-150-200	-2	50	$6.9 \times 10^{-4}$	<i>Nat. Mater.</i> , <b>2012</b> , 11, 963
MoS <sub>2</sub> nanoparticale on graphene *	0.28	0.10	-48	41	-	<i>JACS</i> , <b>2011</b> , 133, 7296.
MoS <sub>2</sub> on mesoporous Graphene *	0.21	-100	-30–40	42	-	<i>Adv. Funct. Mater.</i> <b>2013</b> , 23, 5326.
MoS <sub>2</sub> on graphene/Ni foam	11.7	-	-44	42.8	-	<i>Adv. Mater.</i> <b>2013</b> , 25, 756
MoS <sub>2</sub> on Ti *	0.12	250	-30	51	$3.87 \times 10^{-4}$	<i>Adv. Mater.</i> <b>2014</b> , 26, 2683
MoS <sub>2</sub> on TCNQ on carbon cloth	3.41		-209	40		<i>Appl Mater Int.</i> , <b>2014</b> , 85, 17679
MoO <sub>2</sub> on N-doped MoS <sub>2</sub>	0.285	-156		47.5	-	<i>J. Mater. Chem. A</i> , <b>2014</b> , 2, 11358
MoS <sub>2</sub> /nitrogen-doped graphene *	-	0.236	-10	230	-	<i>J. Mater. Chem. A</i> , <b>2014</b> , 2, 13795

**Note:** The data calculated after the  $iR$  correction are marked by \*.